


Interaction of a buoyant plume with a turbulent canopy mixing layer

Hayoon Chung * and Jeffrey R. Koseff*Department of Civil and Environmental Engineering, Stanford University, Stanford, California 94305, USA*

(Received 17 October 2022; accepted 4 May 2023; published 23 June 2023)

This study aims to understand the impact of instabilities and turbulence arising from canopy mixing layers on wind-driven wildfire spread. Using an experimental flume (water) setup with model vegetation canopy and thermally buoyant plumes, we study the influence of canopy-induced shear and turbulence on the behavior of buoyant plume trajectories. Using the length of the canopy upstream of the plume source to vary the strength of the canopy turbulence, we observed behaviors of the plume trajectory under varying turbulence yet constant cross-flow conditions. Results indicate that increasing canopy turbulence corresponds to increased strength of vertical oscillatory motion and variability in the plume trajectory/position. Furthermore, we find that the canopy coherent structures characterized at the plume source set the intensity and frequency at which the plume oscillates. These perturbations then move longitudinally along the length of the plume at the speed of the free stream velocity. However, the buoyancy developed by the plume can resist this impact of the canopy structures. Due to these competing effects, the oscillatory behavior of plumes in canopy systems is observed more significantly in systems where the canopy turbulence is dominant. These effects also have an influence on the mixing and entrainment of the plumes. We offer scaling analyses to find flow regimes in which canopy induced turbulence would be relevant in plume dynamics.

DOI: [10.1103/PhysRevFluids.8.064501](https://doi.org/10.1103/PhysRevFluids.8.064501)

I. INTRODUCTION

Despite the increasing frequency and severity of extreme and devastating wildfire disasters in the past couple decades [1–5], the technology or infrastructure for combating them has been inadequate and expensive [6]. Furthermore, detailed physical understanding of wildfire spread in many areas is not complete. As a result, current physical models that incorporate meteorology, flow physics, and combustion physics are unable to accurately predict fire-spread conditions. Observations of wildfires find more extreme behavior such as rapid spread, mass ignition, or spotting over distances of miles to be more prevalent [7]. Of the many knowledge gaps pertaining to wildfire spread and physics, understanding plume dynamics perhaps has a great potential for improving our understanding of wildfire behavior and for predicting their rate of spread. Therefore, it is crucial for those responsible for wildfire management to better understand plume dynamics and associated spotting [7].

Plumes in wildfires refer to the hot columns of air that rise from the fire that are capable of convective mass and heat transfer. Hot buoyant plumes enhance wildfire spread by drying out downwind fuel through convective heat transfer [8], and by creating updrafts and subsequent extreme mechanics and vorticity [7,9], and transporting embers that ignite new unburnt fuel downwind [10–13]. Previous studies in wildfire literature find that behavior of these buoyant plumes depends heavily on interaction with the ambient mean flow [14–16] but not with the ambient turbulence [17,18]. The latter studies [17,18] found that atmospheric turbulence and other ambient turbulence is negligible compared to the strong turbulence intensities generated internally by the plumes.

*hayoonch@stanford.edu

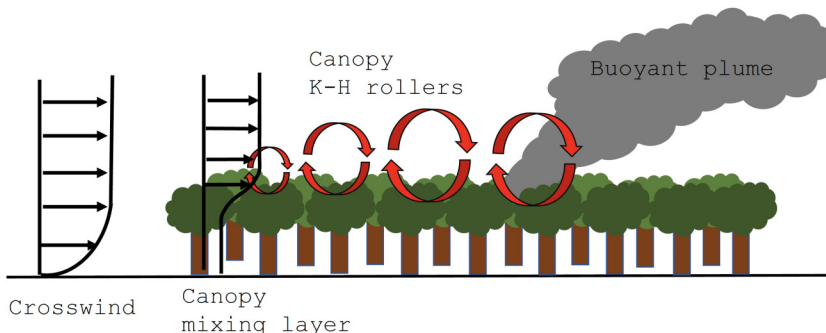


FIG. 1. Visual representation of a canopy mixing layer developing over a forest canopy. The buoyant plume is introduced at some distance along the canopy and interacts with the Kelvin Helmholtz rollers.

Additional plume studies find that bent-over plumes can be sensitive to ambient turbulence for entrainment and mixing [19–21]. While atmospheric or other ambient turbulence may have limiting impact on plume behavior, we hypothesize that a different source of turbulence, canopy mixing layers (ML) (commonly observed in forests), can have a strong impact on the plume dynamics. This is because the physical scale associated with canopy mixing layers is comparable to that of the plume. A visualization of a buoyant plume in a canopy mixing layer is provided in Fig. 1. Because the turbulence associated with canopy mixing layers is distinct, we predict that its impact on the plume behavior will be distinguishable from that of other more extensively studied ambient turbulence such as isotropic or boundary layer [18] turbulence. Thereby, this study focuses on how, in particular, a buoyant, bent-over plume behaves in a canopy mixing layer.

Bent-over buoyant heated plumes, which comprise the first element of this study, have been extensively studied in the past for varying applications. Examples include smokestacks, sewage outfalls, and volcanic plumes [17,22–30]. The extensive research on plume behavior was motivated by the multitude of engineering problems that involve the dilution or containment of sources (plumes) of mass within the environment. Examples include the Brigg’s plume rise model [31] and other studies that build on the understanding of plume behavior, height, deflection, mixing, and trajectory. The pertinent work that has been applied extensively in wildfire dynamics is the Roberts [30] study of line sources of buoyant fluid in ocean outfall design [9,14,16,32–36].

The second component of this study involves controlling the ambient mean flow and turbulence into which the plume is being released. Canopy shear dynamics (CSD) refer to the momentum and turbulence balance/budget and flow structure that arise when channel flow adjusts over a canopy (i.e., flow through a forest canopy). CSD, as observed in wind through forest canopies, alter and control the flux of momentum, turbulence, scalars, and heat within canopy systems [37–42]. The resulting fully developed flow profiles are not simple uniform crosswinds or boundary layers above roughness elements but rather a mixing layer characterized by canopy shear and coherent structures [37–39]. The canopy ML wind profile and behavior depend on the mean wind speed, canopy dimension, and canopy density. At high-enough density and wind velocity, the ML contains an inflection point at the canopy top and becomes unstable to Kelvin-Helmholtz (KH) instabilities of frequency f_{KH} . The size of these coherent structures, which form at the interface of the canopy top and overlying wind, can be large enough to potentially impact the buoyant plumes that arise from burning canopies (Fig. 1). While previous studies have looked at the influence of canopy structure on wildfire behavior [9,43–47], they focus primarily on accurately modeling other aspects of wildfire spread (atmospheric physics, combustion, chemical mass flux). Few studies even acknowledge the need to account for or incorporate the effects of the coherent structures of CSD in wind simulations [48]. Therefore, in this study, we specifically examine whether CSD, and its associated coherent structures and turbulence, has an impact on plume trajectory and behavior.

For the system outlined above (as shown in Fig. 1), there needs to be a way of quantifying the strength of each component: plume, cross-flow, and canopy turbulence. For wildfires, this has traditionally been done for plumes and cross-flows using convective Froude numbers such as the Clark Froude number (Fr_c) or Byram's energy criterion (N_c) [14,15,49], which are based on well-established literature for buoyant plumes, as well as jets and plumes from sewage outfalls [30]. Roberts [30] defines a Froude number for ocean diffusers:

$$Fr_R = (u_c^3)/B_R. \quad (1)$$

In Eq. (1), u_c is the ocean current speed and $B_R = g\Delta\rho q/\rho_a$ is the buoyancy flux per unit length. $\Delta\rho$ is the density difference due to the temperature difference at the plume source, q is the source flowrate per unit length, and ρ_a is the ambient density. This expression was adapted for wildfire application by Byram [14] and Nelson [15] leading to the development of the Byram's criterion, $N_c = P_f/P_w = 2gI/[(c_p\theta_a)\rho(u-r)^3]$. N_c compares the power of the plume (vertical momentum and buoyancy), P_f , to the power of the wind (longitudinal momentum), P_w . Representing the buoyancy flux, $gI/(c_p\theta_a)\rho$ includes I (fire intensity), c_p (heat capacity), and θ_a (potential temperature). The advective power is represented by $(u-r)^3$, in which u is the cross-flow velocity and r is the wildfire rate of spread [33]. Because N_c is a form of an inverse Froude number, a fire Froude number, Fr_F , can be given by

$$Fr_F = \frac{u^3}{b_F} = 2N_c^{-1}, \quad (2)$$

in which u is the background velocity and b_F is the buoyancy flux for fires [35]. Because our study does not incorporate real fires, we will use the Froude number in Eq. (1) and the relationship in Eq. (2) to calculate the equivalent N_c for our system.

N_c is also used to characterize wildfires as being either fire/plume dominated ($N_c > 1$) or wind driven ($N_c < 1$) [15,49]. While wind-driven systems often correlate with high rate of spread, various studies have found N_c to be useful in predicting rate of spread, while others found it to be limiting in predictive efforts [33,35,49,50]. However, because no nondimensional number similar to N_c incorporates ambient turbulence in its formulation, our study aims to characterize plume behavior by accounting for turbulence. In summary, the goal of this study is to characterize plume behavior and mixing in the presence of canopy flow structures and turbulence, while suggesting alternative scaling and nondimensional parameters to capture their interaction, and determine when they are relevant.

II. METHODOLOGY

A. Flow setup

Experiments were carried out in a plexiglas water flume with a model vegetative canopy and a gravitationally released heated plume/jet. As shown on Fig. 2(a), a buoyant plume is released from a source placed in a homogeneous canopy. The test section of the flume measures 7.2 m long by 1.4 m wide and 0.4 m deep. We used two flow speeds, (referred to as A and B in Table I) which correspond to depth averaged velocities U of 0.09 and 0.13 m/s, respectively. The model canopy was composed of an array of wooden dowels (cylinders) fastened onto an acrylic sheet (Fig. 2). For all experimental cases, the total canopy length, L_c , was kept constant at 1.6 m. The canopy was homogenous in both spanwise and longitudinal directions with a canopy frontal density of $a = nd = d/(\Delta s^2) = 0.78 \text{ m}^{-1}$, in which the diameter (d) is 6.35 mm and the average spacing between the dowels (Δs) is 2.86 cm. The canopy height was kept constant at 10 cm with a submergence ratio of $h_c/H = 0.25$.

In order to test the impact of CSD on the plume behavior, we varied the canopy turbulence strength and intensity at the plume source. While the total canopy length was kept constant, we varied X_p , the streamwise distance from the leading edge of the canopy to the plume source efflux. This upstream canopy length controls the turbulence conditions, because canopy-induced turbulence develops over a finite length before reaching fully developed turbulence [51–53]. Within

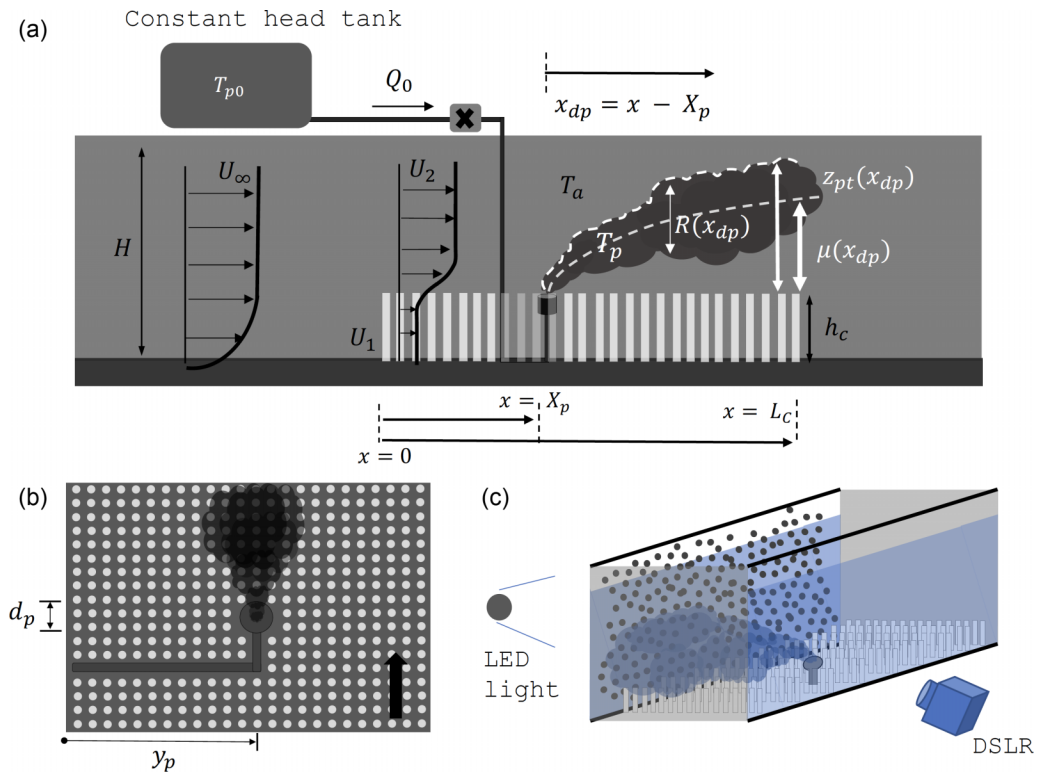


FIG. 2. Diagrams of experimental setup. (a) Side-view of the experimental setup. The flow going from left to right has a free-stream flow speed (U_∞) corresponding to either Flow A or B. On interacting with the canopy, the flow develops an overflow (U_2), through-flow (U_1), and shear layer with an inflection point slightly above the canopy height, h_c . The plume setup, as shown, has PVC piping with fixed flow rate Q_0 . This pvc piping leads to a plume release mechanism at the canopy height. The distance from the leading edge of the canopy to this release point is given by X_p , while the length of the whole canopy is L_c . The temperature of the plume is T_p (a function of x and z), while the ambient is T_a . The trajectory of the plume is given by the distance from the canopy height to the centerline of the plume, $\mu(x_{dp})$, and the upper edge, $z_{pt}(x_{dp})$. The vertical length of the plume is given by $R(x_{dp})$. (b) Plan-view of plume release. y_p is the distance from the flume wall, which is equidistant in either spanwise direction. d_p is the diameter of the plume diffuser. (c) Diagram of the synthetic Schlieren setup. A dotted pattern is placed in the background with LED lighting, so that the camera can track distortions caused by the plume's density gradients.

this transitional length, the upstream canopy length will produce turbulence levels that increase monotonically with length [52,53]. Therefore, the plume was released at 0.3, 0.6, 0.9, and 1.2 m from the leading edge of the canopy for the different test cases, as seen in Table I. [For the 1.2 m case, we padded the end of the canopy with 20 cm of canopy (for a total of 1.8 m), to ensure no canopy edge effects impact the plume behavior.] By doing so, the plumes experience a range of turbulence conditions. Velocity and turbulence statistics profiles were measured with a Vectrino+ acoustic doppler velocimeter at these locations above the canopy (without the plume). The velocity records were sampled at 200 Hz, filtered to 50 Hz using a Gaussian filter, and then filtered for outliers based on values greater than 4 standard deviations from the mean. These data were used to calculate mean and turbulence statistics, as well as turbulence spectra, to provide information on the ambient mean and turbulence flow conditions that impact plume behavior.

For each different streamwise positions ($x = X_p$), the plume outlet was placed at the canopy height ($z = h_c$) and at the centerline (in the cross-stream direction) of the flume and canopy

TABLE I. Experimental parameters (n/a, nonapplicable; s/a, same as above). For case names, “A” or “B” denote the flow case. This is followed by “03,” “06,” “09,” and “12” corresponding to X_p of 0.3, 0.6, 0.9, and 1.2 m. Last, dT is followed by the ΔT at the plume source. The table provides the location of plume release, X_p , the source temperature differential, ΔT , and the effective/average vertical velocity of the plume, w_{eff} (described in Appendix B).

Case	Flow	X_p (m)	ΔT (°C)	w_{eff} ($\frac{\text{m}}{\text{s}}$)	u_* ($\frac{\text{m}}{\text{s}}$)	Case	Flow	X_p (m)	ΔT (°C)	w_{eff} ($\frac{\text{m}}{\text{s}}$)	u_* ($\frac{\text{m}}{\text{s}}$)
A03dT10	A	0.3	10	0.016	0.0050	A06dT10	A	0.6	10	n/a	0.0059
A03dT20	A	s/a	20	0.018	s/a	A06dT20	A	s/a	20	n/a	s/a
A03dT30	A	s/a	30	0.020	s/a	A06dT30	A	s/a	30	n/a	s/a
A03dT40	A	s/a	40	0.021	s/a	A06dT40	A	s/a	40	n/a	s/a
A03dT50	A	s/a	50	0.023	s/a	A06dT50	A	s/a	50	n/a	s/a
A09dT10	A	0.9	10	n/a	0.0078	A12dT10	A	1.2	10	n/a	0.0097
A09dT20	A	s/a	20	n/a	s/a	A12dT20	A	s/a	20	n/a	s/a
A09dT30	A	s/a	30	n/a	s/a	A12dT30	A	s/a	30	n/a	s/a
A09dT40	A	s/a	40	n/a	s/a	A12dT40	A	s/a	40	n/a	s/a
A09dT50	A	s/a	50	n/a	s/a	A12dT50	A	s/a	50	n/a	s/a
B03dT10	B	0.3	10	0.015	0.0065	B06dT10	B	0.6	10	n/a	0.0072
B03dT20	B	s/a	20	0.017	s/a	B06dT20	B	s/a	20	n/a	s/a
B03dT30	B	s/a	30	0.021	s/a	B06dT30	B	s/a	30	n/a	s/a
B03dT40	B	s/a	40	0.022	s/a	B06dT40	B	s/a	40	n/a	s/a
B03dT50	B	s/a	50	0.023	s/a	B06dT50	B	s/a	50	n/a	s/a
B09dT10	B	0.9	10	n/a	0.0091	B12dT10	B	1.2	10	n/a	0.014
B09dT20	B	s/a	20	n/a	s/a	B12dT20	B	s/a	20	n/a	s/a
B09dT30	B	s/a	30	n/a	s/a	B12dT30	B	s/a	30	n/a	s/a
B09dT40	B	s/a	40	n/a	s/a	B12dT40	B	s/a	40	n/a	s/a
B09dT50	B	s/a	50	n/a	s/a	B12dT50	B	s/a	50	n/a	s/a

($y_p = 0.6$ m). The plume source (outlet) diameter, D , is 1.9 cm. A constant head tank located above the flume gravitationally releases heated water from the plume outlet at a flow rate of $Q = (5.99 \pm 0.2) \times 10^{-5}$ m³/s. The constant head tank is an insulated beverage dispenser converted into a Mariotte’s bottle [Fig. 2(a)]. The source is connected to the plume outlet through pvc piping fitted with valves for controlling the flow rate and separately for opening/closing the connection to the constant head tank. The temperature in the tank was found to remain constant over the duration of an experiment, and the temperature of the heated jet measured at the plume outlet revealed that there was no measurable heat loss through the PVC piping between the tank and outflow. For each of the different background flow conditions (mean flow velocity and varying X_p), we tested plumes characterized by $\Delta T = T_s - T_a$ of 10° to 50°C, in which T_a is the ambient water temperature and T_s is the plume source temperature (Table I). These conditions provide for the five different source buoyancy conditions that correspond to densimetric Froude numbers, $Fr_s = w_0/\sqrt{g'A^{1/2}}$, of 10.1 ($\Delta T = 10^\circ\text{C}$), 6.9 ($\Delta T = 20^\circ\text{C}$), 5.3 ($\Delta T = 30^\circ\text{C}$), 4.3 ($\Delta T = 40^\circ\text{C}$), and 3.7 ($\Delta T = 50^\circ\text{C}$). In this expression, w_0 is the source exit flow vertical velocity, g' is $g\frac{\rho_s - \rho_a}{\rho_a}$, for which ρ_s is the density of the plume at the source and ρ_a is the density of the ambient fluid, and A is the source cross-sectional area.

B. Plume imaging and tracking

To track the plume’s trajectory and behavior, we utilized synthetic-Schlieren, or background oriented Schlieren methods [54] instead of dye. As shown in Fig. 2(c), over the test section (a length of 0.8 m) a backdrop of random dot patterns of different sizes (printed on backlit film) covered the glass flume side-wall. LED lights controlled the lighting from behind the backdrop. A DSLR

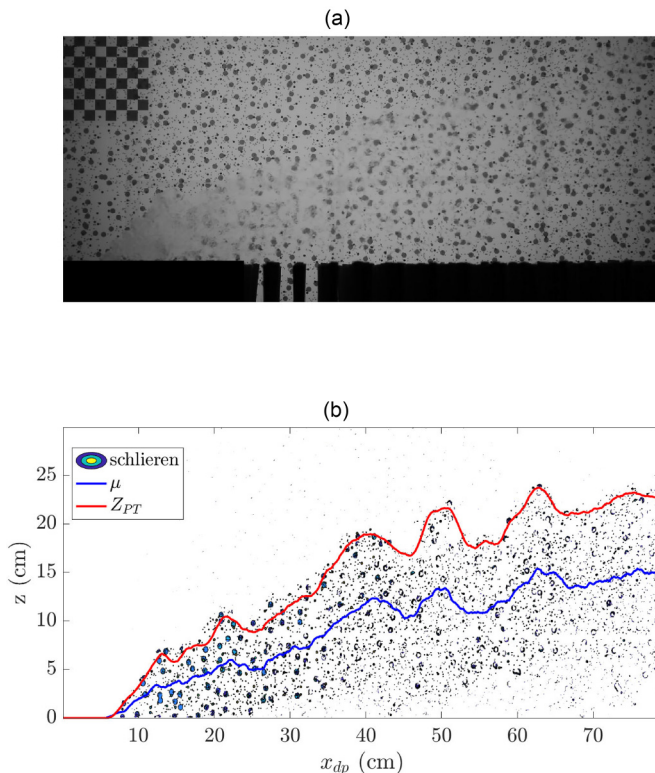


FIG. 3. Schlieren methodology: (a) Raw image of plume release with heated plume in front of dot pattern. (b) Schlieren image with background subtraction, and outline of centerline, μ , and plume top, z_{pt} in blue and red, respectively. The z axis, z , is in cm above the canopy top.

camera was used to capture images of the plume and dot-pattern background from the opposite side of the flume. When the dot-pattern background is observed through the fluid, any density gradients create distortions of the image behind due to alteration of the index of refraction [54]. The distortions can be observed through shimmers, dilations, blurring, and shifts in the stationary background across frames. Using such distortions, we can identify regions of the flow that contain buoyant (thermally) fluid. While this method can be extended with particle image velocimetry (PIV) algorithms to realize actual density fields, we only extracted the outline of the plume over time. This was done by subtracting the base image (background with no distortions) from the experimental plume visualization, which provides a rough outline/shape of the plume as seen in Fig. 3(b). This figure shows that regions with stronger Schlieren (hotter fluid) displaces the larger dots, while regions with weaker Schlieren displaces the smaller dots and fractions of the larger dots.

Using the outline of the plume represented by the dot pattern, we can approximate the upper and lower boundaries of the plume, and thereby determine the plume centerline, at any instant in time as shown on Fig. 3(b). To approximate these, we statistically analyzed each vertical segment (unit pixel width) of pixel intensity in the subtracted image. The approximated trajectories (in x) started from the source start point ($x = X_p$) and extended 0.72 m downstream. The coordinate system relative to the source point is given by $x_{dp} = x - X_p$, or the distance from the plume source [Fig. 2(a)]. The upper boundary was set at the maximum position of nonzero pixel intensity, after removing outliers using Matlab's outlier detection algorithm. Assuming that the plume maintains a Gaussian distribution of thermal concentration in the radial direction, we located the centerline by calculating the position of the centroid the distribution of each vertical transect. The centroid is defined by

$\mu(x_{dp}) = M_1/M_0 = (\int P_i * z dz) / (\int P_i dz)$, in which M_i are the moments, P_i is the pixel intensity, and z is the vertical coordinates in pixels. Figure 3(d) provides an example of these extracted plume outlines and trajectories overlaying the Schlieren imaging. Using this method, we are able track the plume's centerline, μ , and upper boundary, z_{pt} , as a function of x_{dp} over time. We can also use this method to calculate the radius, $R(x_{dp}) = 2 * \sigma$, of the plume along its length [Fig. 2(a)] using the moments for the variance, $\sigma^2 = M_2/M_0 - \mu^2 = \frac{\int P_i * z^2 dz}{\int P_i dz} - \mu^2$. In this case, we treat the vertical length of the plume perpendicular to the plume bottom (rather than the plume centerline) as the plume diameter. Each experimental case was 7 min long, with a sampling rate of 60 Hz. The statistics discussed in the results section are found to converge after 4 to 5 min.

Sources of uncertainty for this estimation of either μ or z_{pt} using this method arises from the resolution of the random dot pattern. Due to the spacing, there are pixel locations at which a dot, or fragment of a dot, does not exist at the interface between the plume and ambient flow. As a result, the outline of the upper edge of the plume, and thereby the distribution of the dots for deriving μ , can be underestimated. The plume trajectories that are presented in the results section are processed from the raw trajectories by removing these outlier positions, and replacing them via linear interpolation, and then smoothing with a Gaussian filter. As a result of this smoothing, as seen in Fig. 3, the upper edge of the plume (in red) can miss the plume edge. The over or under-approximation of the plume edge tend to be at most around 1.5 cm. To estimate this uncertainty, we quantify at each pixel position, the spatial standard deviation of the raw/un-smoothed plume trajectory across a 2 cm width (streamwise). This allows us to quantify how much average deviation in the plume vertical position there may be, from the smoothed/processed position.

III. RESULTS

A. Flow background

Before observing the influence of varying canopy turbulence on plume behavior, we characterized the canopy turbulence with velocity profiles. This is the flow and turbulence observed in the ambient without the plumes. In Fig. 4(a), for both Flow A and B speeds, we plot the velocity and Reynolds stress profiles measured above the canopy height. The streamwise velocity profiles are taken at each X_p location. The profiles show that the mean streamwise velocity, $\bar{U}(z)$, and the turbulence, evolves as the flow adjusts to the canopy elements (over x). However, while the magnitude of the shear in the shear layer varies minimally, the turbulence continues to grow monotonically. As found in previous studies on developing canopy-shear turbulence, this is because the velocity reaches a fully developed state sooner (over shorter canopy length) than the turbulence [both the Reynolds stress (RS) and ke (turbulent kinetic energy)] [52,53]. By design, our X_p (locations where plume is being released) is shorter than the canopy length required for fully developed turbulence. Thereby, with increasing X_p , the heated jet will experience increasing levels of canopy-shear turbulence. This allows us to isolate the influence of only the ambient CSD turbulence strength while maintaining similar mean (cross-flow) conditions. For canopy systems, a way to quantify this growing canopy shear turbulence is a friction velocity, u_* , as provided in Table I. u_* is given by the RS at the canopy height, $u_* = (-\overline{u'w'}|_{h_c})^{1/2}$. Both flow speeds show that u_* increases monotonically with increasing X_p . For the remainder of the paper, we will be using u_* as the velocity scale representing the canopy turbulence.

B. Impact of CSD on plume behavior

Using the image records, we can track the plume behavior as it experiences varying levels of CSD turbulence in the ambient. For each of the experimental cases listed in Table I, we tracked the plumes' top edges (z_{pt}) and centerlines (μ) and analyzed their time records. In Fig. 5 we plot the time mean (over 7-min duration at 60 Hz) of the trajectory realizations for both μ and z_{pt} , across all X_p (varying u_*) cases. It also compares the time-mean trajectory for minimally heated ($\Delta T = 10^\circ\text{C}$)

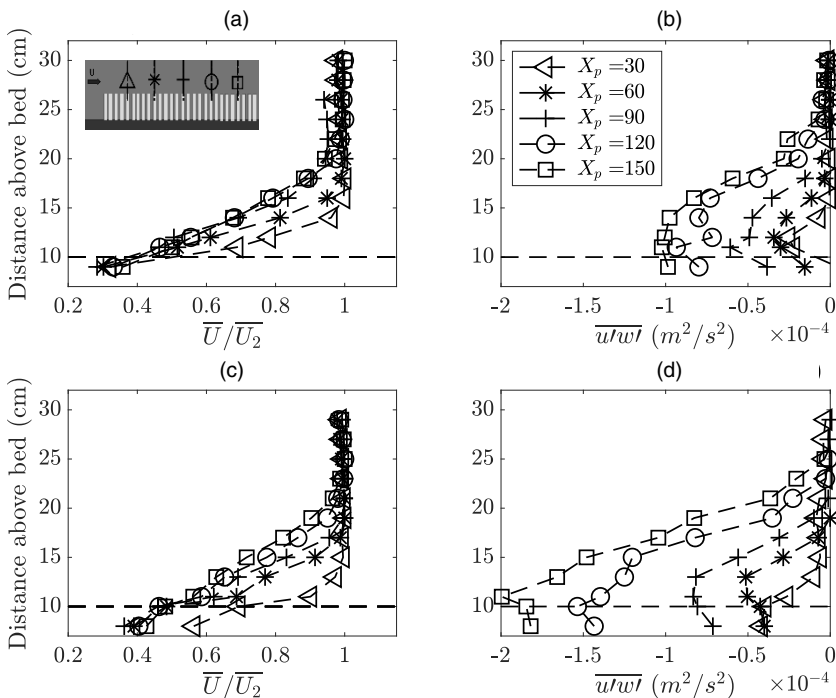


FIG. 4. Mean velocity [(a) and (c)] and Reynolds stress profiles [(b) and (d)] for both flow cases, measured above the canopy height. As on legend, each shape corresponds to distance from the leading edge of the canopy (in cm).

and strongly heated (50°C) plumes for both Flow A and B. For each experimental case, the average uncertainty is found by taking the time average of the uncertainty (as discussed in Sec. II B) found at each point. We provide this estimate for each plotted experimental case, at x_{dp} locations near the head, middle, and tail of the plume. As expected, we can see that the plume under Flow B (faster background cross-flow) is slightly more bent over than that under Flow A. We also observe that the hotter plumes in Figs. 5(b) and 5(d) ($\Delta T = 50^\circ\text{C}$) under the same cross flow velocity experience a steeper trajectory (penetrate higher into the water column) due to buoyancy effects.

More importantly, we observe that for fixed ΔT and cross-flow rate, the mean trajectories do not vary a great deal with varying X_p . In other words, increasing canopy turbulence (u_*) does not significantly alter the time mean position of the plumes. There may be some inaccuracy in the represented plots, because for the more turbulent cases, there were instances in which regions of the plume falls below the canopy height (plume pushed into the canopy) and thereby skew the μ distribution. This is discussed in more detail in Appendix C. Aside from these small variations, the results suggest that with increasing canopy-induced turbulence (u_* increased), the mean trajectory remains largely unaffected.

However, while mean trajectories remain unaffected, instantaneous plume trajectories show significant effects of canopy turbulence. Figure 6 shows individual realizations of the plume centerline over a period of 45 s, in 4-s intervals. Figures 6(a) and 6(b) are for Flow A while Figs. 6(c) and 6(d) are for Flow B. For the same cross-flow, Figs. 6(a) and 6(c) are for the lowest turbulence at the source ($X_p = 0.3$ m), while Figs. 6(b) and 6(d) are for the maximal turbulence ($X_p = 1.2$ m). For reference, the ambient mean and turbulence levels that these plumes experience can be found through the \bar{U} and RS profiles on Fig. 4(a). We can observe that for the $X_p = 0.3$ m versus $X_p = 1.2$ m cases (for both Flow A and B), the cross-flow in the shear layer are similar, but the RS values are drastically different.

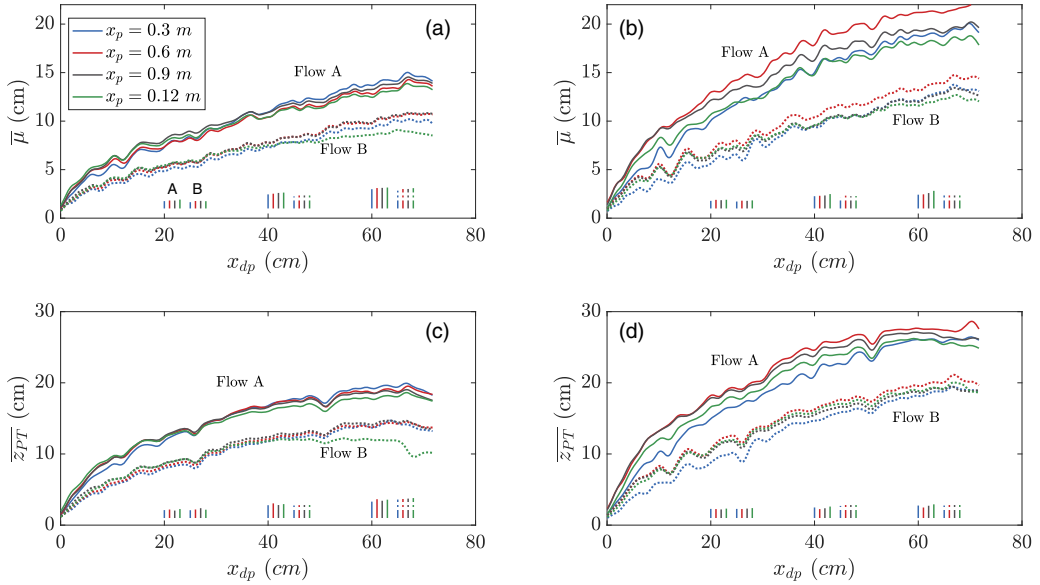


FIG. 5. Time mean trajectory for various experimental cases. The x axis represents the streamwise distance from the plume outlet (x_{dp}) while the z axis represents the plume position (cm above canopy top). [(a) and (b)] The position of the centerline, μ , and [(c) and (d)] the plume-top z_{pt} . The left and right columns are for cases with source plume temperature of $\Delta T = 10^\circ$ and 50°C , respectively. The solid lines correspond to Flow A cases while the dotted lines correspond to Flow B cases. The colors correspond to different turbulent conditions (X_p). Uncertainty: Below the plots, we provide the average uncertainty for each experimental case, as observed for the trajectories at x_{dp} of 20, 40, and 60 cm. The Flow A cases are in solid lines while the Flow B cases are given by the dotted lines. Each color corresponds to the different X_p cases as in the legend.

Figure 6 shows that the vertical plume position downstream of the plume outlet fluctuates about some mean position over time. Plumes under cross-flow with small ambient turbulence will still experience natural variation due to the shear between the plume and ambient, as well as additional instabilities/circulation cells caused by buoyancy [27]. This natural variation is most closely represented by the $X_p = 0.3$ m cases in Fig. 6(a) and 6(c). With these cases, canopy-induced turbulence is small at the plume source because the canopy turbulence is just beginning to develop. For the rest of the study, the cases with $X_p = 0.3$ m will, therefore, be used as the base case with no CSD impact for comparison purposes.

When comparing the A03dT50 case [Fig. 6(a)] to the A12dT50 case [Fig. 6(b)], or the B03dT50 case [Fig. 6(c)] to the B12dT50 case Fig. 6(d)], we observe that there is much more vertical variability in the latter cases. This is most strongly observed in the B12dT50 case. For example, the instantaneous trajectory centerline for B12dT50 at $t = 4.5$ s (light blue) is distinctly different from that at $t = 45.8$ s (black line), in that the position of centerline has changed by almost 17 cm over 40 s. The former reaches up to the 22 cm above the canopy top at $x_{dp} = 60$ cm while the latter is closer to 5 cm at the same position. This is in stark comparison to the B03dT50 case where the mean μ at the same X_p location remains at around 10 cm over the entire time period. These results suggest that plumes under strong CSD (longer X_p) will experience more vertical variability (over time) and therefore much more extreme instantaneous plume heights (much higher and lower). When observed as a video, the plumes variability under strong CSD turbulence manifests as vertical oscillatory motion of the entire plume (from head to tail). Similar trends can be observed for the other experimental cases.

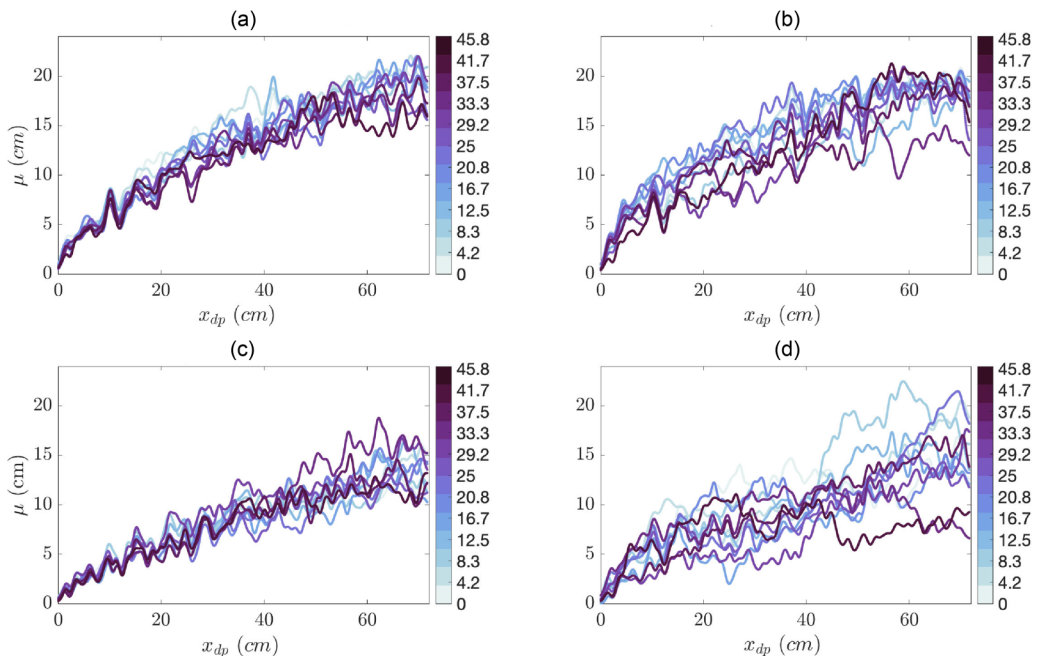


FIG. 6. Instantaneous plume trajectory centerlines μ for different cases over 45 s. The color bar ranging from light blue to dark purple corresponds to seconds, from 0 to 45 s. All cases plotted are for $\Delta T = 50^\circ\text{C}$ source plumes. Panels (a) and (b) compare the $X_p = 0.3$ m case to the 1.2-m case for Flow A (A03dT50 to A12dT50). Panels (c) and (d) repeat it for the Flow B case (B03dT50 to B12dT50). The units of the colorbar are in seconds. Although not plotted, uncertainty in these instantaneous realizations of the plume trajectory is at maximum around 3 cm.

Figure 6 only compares the most extreme CSD cases (most limited and most active) to show that canopy turbulence has a strong influence. However, we observe that other less extreme cases of CSD also have an impact on the plume trajectory and their vertical variability. To better compare this vertical variability across different experimental cases, we introduce new parameters, s_μ/\bar{Z} and s_{pt}/\bar{Z} . \bar{Z} is the time-mean value of the plume position. These two variables are normalized standard deviations of the plume centerline trajectory, $\mu(x_{dp})$ and plume top, $z_{pt}(x_{dp})$. In effect, the standard deviation in the vertical plume position over time represents the strength of plume fluctuation due to the presence of canopy turbulence. The standard deviation is then normalized by the time-mean position of the centerline (μ) or plume edge (z_{pt}). We provide this statistical quantification for one location ($x_{dp} = 11$ cm), in Fig. 7.

Figure 7 shows values of s_μ/\bar{Z} against normalized u_* to observe the impact of CSD on plume variability. u_* is normalized by the maximal u_* observed for $x = 120$ cm, and therefore varies up to 1. Both Flow A and Flow B cases are provided. We observe that with increasing friction velocity (longer X_p), the variance in the plumes' vertical position increases monotonically, and fairly linearly. This shows that as the ambient turbulence due to the development of canopy shear dynamics increases, the plume fluctuates/oscillates up and down more energetically. However, because the friction velocity u_* (or RS) stops increasing once the canopy turbulence becomes fully developed, we predict that the fluctuating energy will asymptotically reach a steady state with longer X_p . Although not plotted, this monotonic linear trend can be observed for the statistics observed at all locations along the plume (other x_{dp}).

Taken together, Figs. 5 and 7 suggest that with stronger canopy turbulence, the mean plume trajectory (μ or z_{pt}) remains the same while the temporal variance increases. To better understand

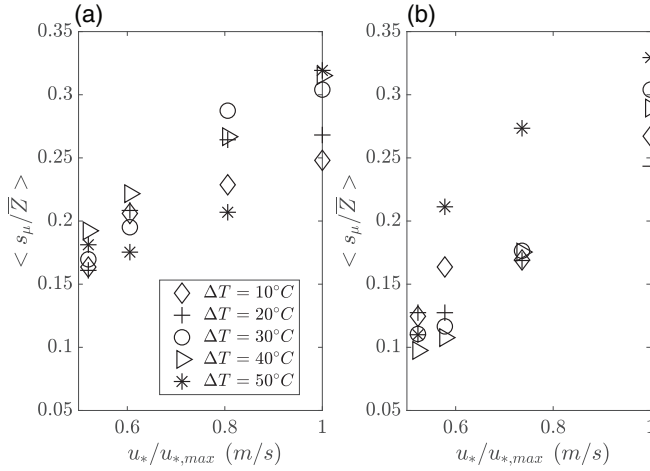


FIG. 7. Plume height variability (s_μ) against normalized friction velocity (u_*). The friction velocity is normalized by the maximal friction velocity observed for each flow rate (which is the u_* measured at $x = 120$ cm). The plotted variability is observed at $x_{dp} = 11$ cm or 11 cm downstream from the plume release. Panels (a) and (b) plot correspond to Flow A and B, respectively. Each symbol corresponds to different source temperature in ΔT .

the distribution of these statistics, we plot the pdf of the trajectory time records for B03dT50 (blue bars) and B12dT50 (orange bars) in Fig. 8. The basis for this comparison is the same plume and cross-flow conditions but different canopy turbulence levels.

For each comparison, we observe that the low and high turbulence test cases have similar μ values corresponding to peaks in the pdf. The base case with limited canopy turbulence, A/B03dT50, has a narrow and somewhat Gaussian distribution. This is because without strong CSD turbulence, the plume maintains its natural mode of small random fluctuations that may mainly be due to shear

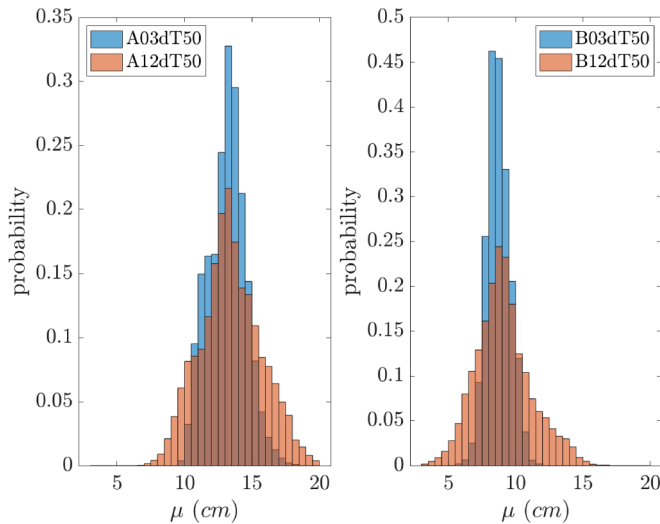


FIG. 8. Probability density function of the time record of plume heights [$\mu(x_{dp} = 32.4$ cm)] for various flow and turbulence cases. The left and right plots correspond to Flow A and B, respectively. The blue and orange bars correspond to $X_p = 0.3$ and 1.2 m, respectively.

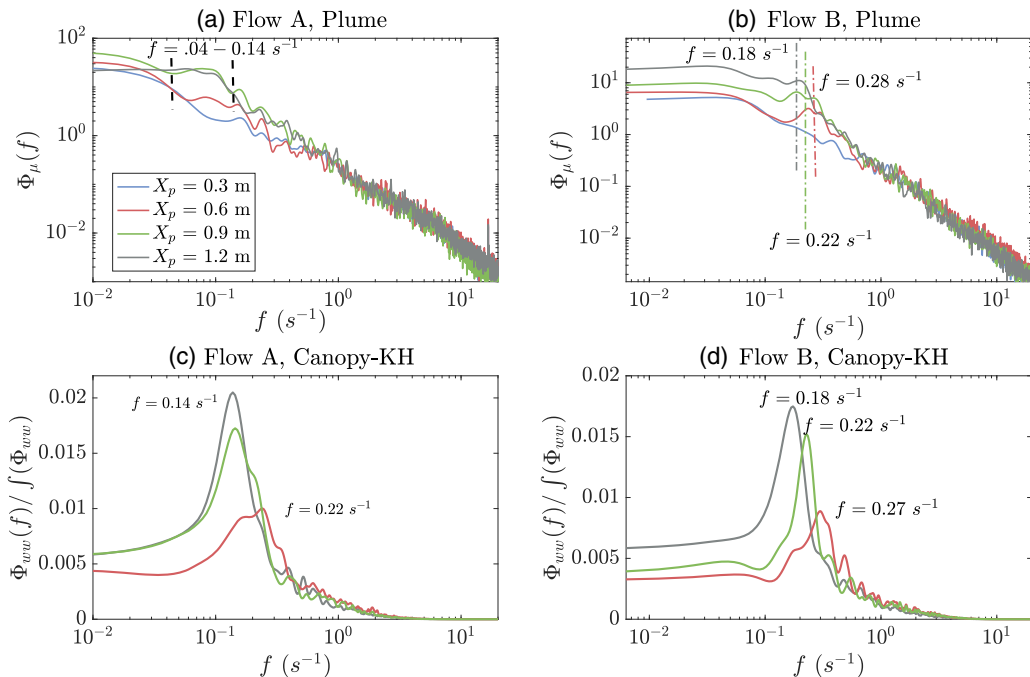


FIG. 9. Spectra for the time records of μ fluctuations, $\phi_\mu(f)$, and for vertical velocity fluctuations, $\phi_{ww}(f)$. The spectral calculation for μ uses the deviation from the mean, $\mu - \bar{\mu}$. The left [(a) and (c)] and right [(b) and (d)] columns correspond to Flow A and B, respectively. The top row plots the spectra measured for $\mu(x_{dp} = 32.4 \text{ cm})$ for varying X_p conditions, in a log-log plot. For all cases, the source plume is characterized by $\Delta T = 50^\circ \text{C}$. The bottom row plots the vertical velocity spectra, also measured at various X_p locations in a log-linear plot, as shown in the legend in plot (a). The velocity spectra for $X_p = 0.3 \text{ m}$ (blue line) is omitted because no peak is observable.

produced by the interaction of the plume with the cross-flow. This suggests that plumes under limited canopy turbulence spend an equal amount of time slightly above and below the mean path. Contrastingly, the spread of A12dT50 or B12dT50 case ($X_p = 120 \text{ cm}$) is much wider, showing that the plume spends much more time at significantly higher (and lower) elevations. This suggests that while the mean cross-flow velocity sets that mean position/trajectory of the plume, the background canopy turbulence adds strong vertical fluctuations about this mean.

While we find that the intensity of vertical fluctuations increases with increasing canopy-induced turbulence (X_p or u_*), one could argue that such results can apply to any random turbulence and not specifically CSD. However, CSD is distinguished from random turbulence in that the flow and turbulence display coherence and organized behavior through the development of KH vortices. These large-scale structures are related to the dominant instability mode formed by the mean mixing layer velocity profile. Therefore, we can analyze patterns in the plume oscillatory behavior to check for a response to the canopy signal. In other words, we want to confirm that the observed large-scale fluctuations are indeed caused by the canopy KH rollers. To do this, we conducted spectral analyses of the plume-path time records [$\mu(t)$] and compared them to spectral analyses of the velocity records taken at each X_p (same measurements/profiles as in Fig. 4). By doing so, we compare the dominant frequency of fluctuation in the plume vertical position to the canopy-roller frequency, f_{KH} .

Figures 9(a) and 9(b) show the spectra for the plume vertical variability (ϕ_μ) measured at $x_{dp} = 32 \text{ cm}$ for both flow speeds. Figures 9(c) and 9(d) show the normalized spectra for vertical velocity fluctuations (ϕ_{ww} , from velocity measurements) measured about 3 to 5 cm above the canopy top,

also for both flow speeds. Each plot compares the spectra for all four X_p cases. For the velocity spectra [Figs. 9(c) and 9(d)], the $X_p = 0.3$ m case was omitted because no spectral peak can be observed. From Figs. 9(c) and 9(d) we can see that the frequencies of the KH rollers for our canopy system's fully developed flow is $f_{KH} = 0.14$ s⁻¹ and 0.18 s⁻¹ for Flow A and B, respectively. However, because the turbulence for some shorter X_p locations is underdeveloped, the f_{KH} is higher in these cases. For example, the f_{KH} measured for Flow B decreases from 0.27 s⁻¹ for $X_p = 0.6$ m to 0.18 s⁻¹ for $X_p = 1.2$ m (Fig. 9). This is most likely because the “rollers” are smaller in size and have higher frequencies before they are fully developed.

The plume spectra [Fig. 9(a) and 9(b)] are based on the fluctuations of μ about its mean over a 7-min duration. These plots reveal how the energy related to plume oscillatory behavior evolves with different canopy turbulence development. Over all the cases, the energy at lower frequencies (large scales) increases monotonically with increasing canopy turbulence (increasing X_p). This is expected because as observed in Fig. 7, the plume variability linearly increases with increasing u_* . And while a strong spectral peak is not observable, we find that the increase in energy is centered about a dominant frequency. For example, in Fig. 9(b), there is no dominant frequency between $f = 0.15$ s⁻¹ and 0.3 s⁻¹ for the flow with limited canopy turbulence ($X_p = 0.3$ m, blue line). However, each subsequent X_p cases display higher levels of energy centered about 0.28 s⁻¹, 0.22 s⁻¹, and 0.18 s⁻¹, respectively, as shown on the legends. For $X_p = 1.2$ m, the dominant frequency is centered about $f_p = 0.18$ s⁻¹. Furthermore, for the Flow B case, we find that the frequency at which the large-scale oscillations grow is the frequency of the instability (f_{KH}) measured at X_p , the plume source. This trend is not observable as distinctly for Flow A. Even so, we find that the range over which enhanced energy is found in the lower frequency spectra ($f_p = 0.4$ –0.14 s⁻¹) overlaps with the measured f_{KH} of $f = 0.14$ s⁻¹. These results are significant in showing that the plumes' large-scale oscillations fluctuate dominantly at the frequency of the rollers that begin to interact with it at its source.

C. Physical properties of the plume under CSD

In this section, we quantitatively characterize the behavior of plumes that are under strong influence of CSD. We distinguish “CSD influence” based on results from the previous section: observable vertical oscillations that grow in intensity at f_{KH} . Given the distinguishing characteristics of canopy turbulence compared to other sources of turbulence, its impact on plume behavior can have implications for transport of momentum, heat, and scalars in wildfire systems. Therefore, we analyze the downstream propagation speed of the flow perturbations within the plume, effects of the plume buoyancy, and mixing and entrainment. Understanding these characteristics will help us identify the potential impact of CSD on wildfire plume dynamics.

1. Propagation speed

For this analysis, we are interested in how information or flow perturbations propagate along the length of the plume. In other words, how do different regions of the plume respond, and at what rate, to the perturbations imparted by the canopy turbulence? We have previously found that plumes under CSD turbulence oscillates strongly above and below the mean path. However, these “oscillations” do not necessarily mean the entire plume, at one instance in time, is displaced upward and downwards. Instead, as seen in Fig. 10(a), the plume becomes distorted. While the time-mean paths plotted in Fig. 5 show smooth, typical bent-over plume trajectories, the instantaneous trajectory on Fig. 10(a) has large dips and peaks to create a more wavelike trajectory outline. This suggests that whole length of the plume at one instant in time is responding to more than one flow perturbation (i.e., more than one distinct canopy roller/event). Such large dips and peaks first originate near the source, then advect downstream at some finite rate.

The observed behavior suggests there are two possible ways the canopy-rollers interact with the plume. First, it may be that when a canopy roller advects downstream and reaches the plume source (at X_p), it perturbs the plume and continually changes the successive pathways of the plume. Because canopy rollers cause alternating upward (ejection-like) and downward (sweeplike) turbulent bursts

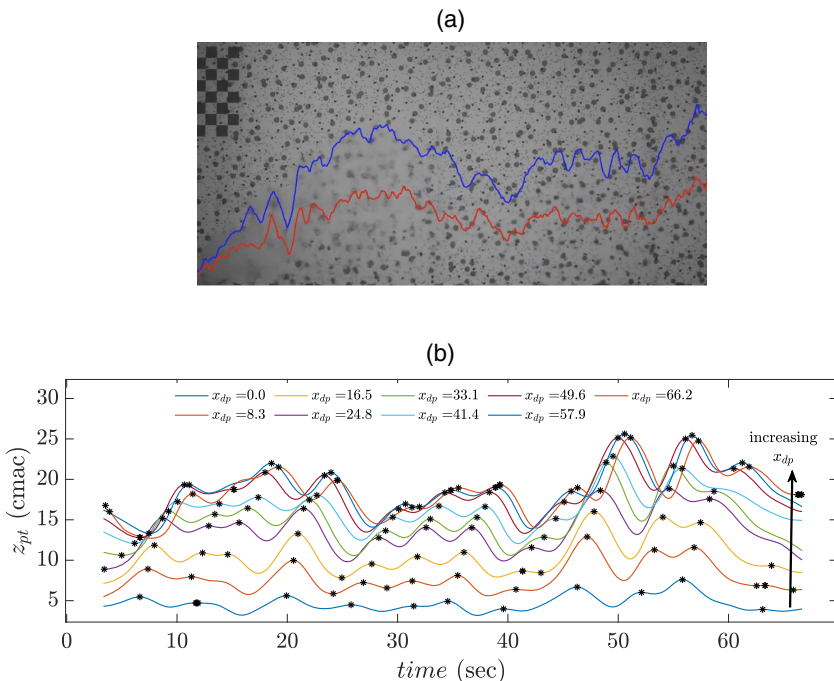


FIG. 10. (a) An example of the plume and its outline (z_{pt} at an instant in time when the trajectory is strongly distorted. This snapshot is from the B12dT50 experimental case. (b) Time record of μ over 70 s for various streamwise location ranging from $x_{dp} = 0$ to 66 cm. The units for the legend are in cm. Local maximum data points are marked with black dot symbols.

in momentum [55], the plume’s source can experience an upward or downward deflection that manifests as oscillations that advect downstream. Alternatively, the distortion may be due to the direct impingement of the advecting canopy vortices on the plume body. The impingement will cause a local deflection in the plume that will advect downstream as the vortices advect downstream at some finite velocity.

To assess which process is causing the asynchronous behavior of the plume length, we extract a “propagation speed,” U_{pl} of the perturbations. This is the speed at which distinguishable features on the plume (CSD perturbations) are transported longitudinally along the plume. In Fig. 10(b), we plot the time record of plume-top vertical position, $z_{pt}(t)$, for various locations along x_{dp} . Similarly to a wave gauge, this provides an Eulerian tracking of the plume height at a fixed point in x . Each of the differently colored lines represent the time records at various streamwise locations over $x_{dp} = 0$ to 66.2 cm. We observe fluctuations in the plume height time record as the roller-induced oscillations (such as the large dips and peaks in the instantaneous trajectory) pass by each point. Interestingly, each of these large distortions detected near the plume head ($x_{dp} = 0$) remain identifiable in the time record for all the locations downstream, with a time shift. Here, we assume that these persisting distinguishable features correspond to the same flow perturbation/event that is advecting downstream. As a result, these locally distinguishable features that manifest as local maxima/minima can be tracked over time and longitudinal distance to understand how they are transported downstream. To visualize this, we marked the distinct features (local maxima) with black stars (*) that can be tracked from one time series to the next [Fig. 10(b)].

To extract the speed at which these features move in x , we present a Hovmoller plot of the plume position in the x - t plane [Fig. 11(a)]. For each distance $x_{dp} = 0$ to 61.6 cm in 1-cm intervals (y axis), a contour of the normalized plume-top position over time is provided (x axis). The plume position

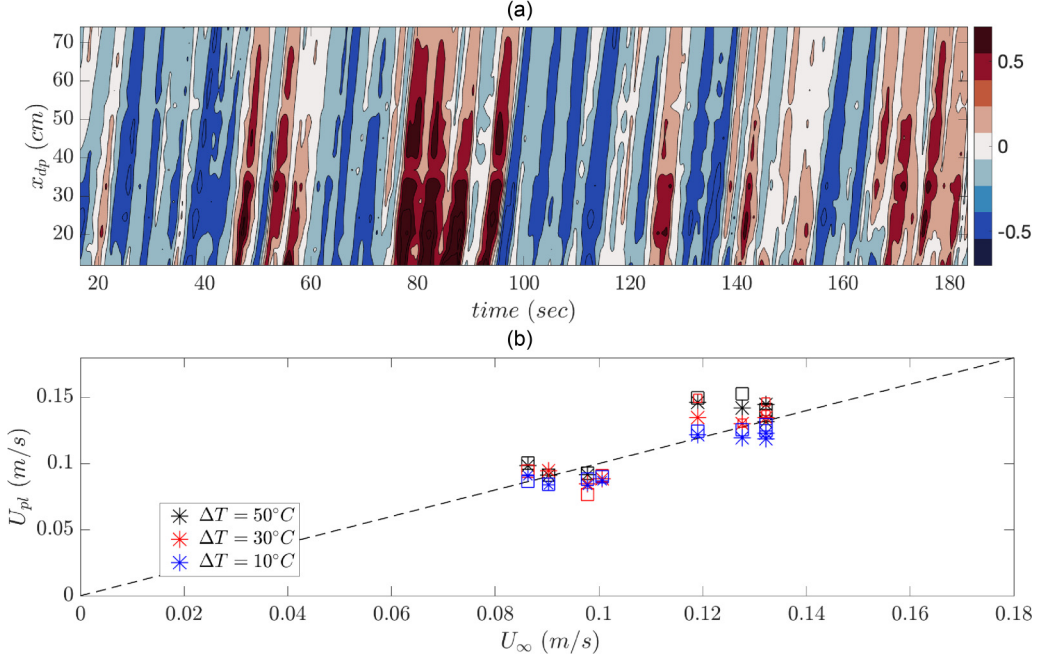


FIG. 11. (a) A contour of the plume-top position normalized by mean height, $(z_{pt} - \bar{z}_{pt})/\bar{z}_{pt}$ in the x - t plane. The red corresponds to local max while blue corresponds to local min. (b) Plot comparing the plume feature propagation velocity, U_{pt} to the free stream velocity, U_∞ . The extracted values of U_{pt} are for $X_p = 0.3, 0.9, 1.2$ m cases. The cluster of point on the lower end is for Flow A, and those on the higher end are for Flow B. Each symbol color corresponds to different ΔT cases, while the star and square symbols correspond to values are for tracked troughs and peaks, respectively. The black dotted line provided is a 1:1 plot.

$z_{pt}(x_{dp}, t)$ is normalized to be centered about zero through the relationship $(z_{pt} - \bar{z}_{pt})/\bar{z}_{pt}$. By centering the data about zero, we can distinguish local minima and maxima by defining them to be above and below the mean, respectively. In Fig. 11(a), the maxima are represented in red while the minima are represented by blue. Each alternating blue or red tracks show that the local features move linearly over x in time. Therefore, similarly to characteristic curves, the slope of these tracks can be used to estimate a propagation speed, U_{pt} . For the different experimental cases, we tracked multiple passing distinguishable features over a 5-min duration to get an average propagation speed.

Figure 11(b) plots the extracted propagation speed U_{pt} against the free stream velocity, U_∞ . The star points are for local minima and squares are for local maxima, which were found to have same propagation speeds. Each color is for different plume buoyancy. Although not plotted, no distinct relationship can be found between U_{pt} and u_* . This means that the turbulence strength of the canopy rollers have no influence on the propagation speed of the perturbations. However, Fig. 11(b) shows that U_{pt} corresponded well with the background free-stream velocity. For the Flow A case, which is the cluster of points near $U_\infty = 0.09$ m/s, points fall on the 1:1 line within error. For the Flow B case, the $\Delta T = 10^\circ C$ falls best on the 1:1 line while the remaining cases are slightly above. These cases show that the perturbations advect at speeds slightly higher than the advective free stream velocity.

The trends observed in Fig. 11(b) suggest that the perturbations created by the turbulent rollers due to the canopy shear move through the plume at the mean background free-stream velocity. This shows that the oscillations in the plume trajectory are caused by canopy rollers impinging at the source rather than directly along the canopy body. This is because canopy rollers have been found to advect at U_{hc} , the mean velocity at the canopy height (inflection point) [51]. This velocity is

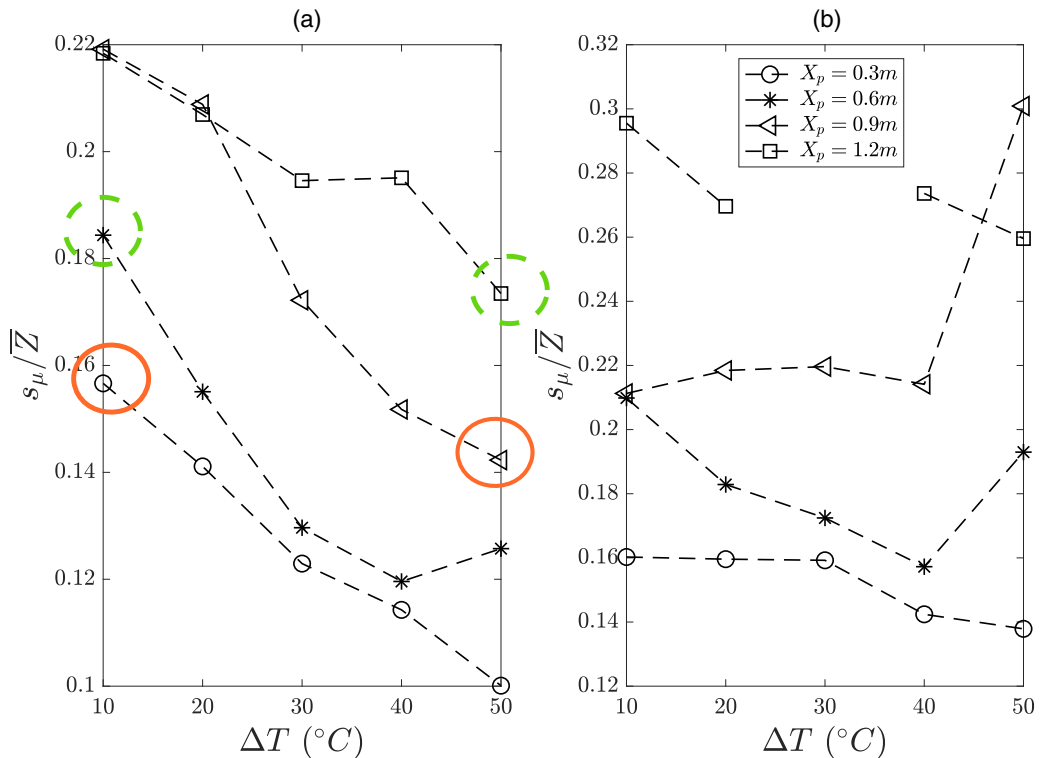


FIG. 12. Variations in plume variability s_μ with source plume temperature for each Flow A and B cases. Each plot provides the values of s_μ measured at $x_{dp} = 32.4$ cm for different ΔT and X_p as shown in legend.

much lower than the observed propagation velocities in Fig. 11. Therefore, the fluctuations that we observe moving along the plume top is caused by canopy rollers imparting a strong imprint on the source/initial conditions of the plume but not by the passage of the rollers themselves downstream. These perturbations (upward and downward deflections) are then expressed through the plume as vertical fluctuations, and are transported at the free-stream velocity.

2. Temperature effects

While we have found that the canopy turbulence characteristics at the plume source have a strong influence on the plume behavior, we have not yet focused on how the plume source conditions have an impact on the interaction with CSD. Because we maintained the same plume source exit velocity (w_0) across all cases, the only varying property was the buoyancy or ΔT . As expected, the mean trajectories of the more heated plumes (higher buoyancy) are angled steeper (Fig. 5). However, we want to see how the buoyancy may have an impact on the expression of the CSD in the plume itself.

In Fig. 12, we plot the variability of the plume centerline, s_μ , as a function of ΔT . (Similar trends were observed for all x_{dp} locations so only one case is shown here.) s_μ is plotted for all canopy turbulence cases for both flow cases. We have previously found that plume oscillatory behavior, s_μ , increases monotonically with increasing canopy turbulence, u_* . However, Fig. 12(a) shows that in the Flow A case, the variability decreases monotonically with increasing ΔT . This can be observed for all canopy turbulence conditions. This effect of increasing ΔT is significant enough that the variability observed for less turbulent cases ($X_p = 0.3$ and 0.6 m) with limited heating ($\Delta T = 10$ °C) is similar to that observed for the more turbulent cases ($X_p = 0.9$ and 1.2 m) with significant heating ($\Delta T = 50$ °C). This is highlighted in the red solid and green dashed circles. Yet, in the case of Flow

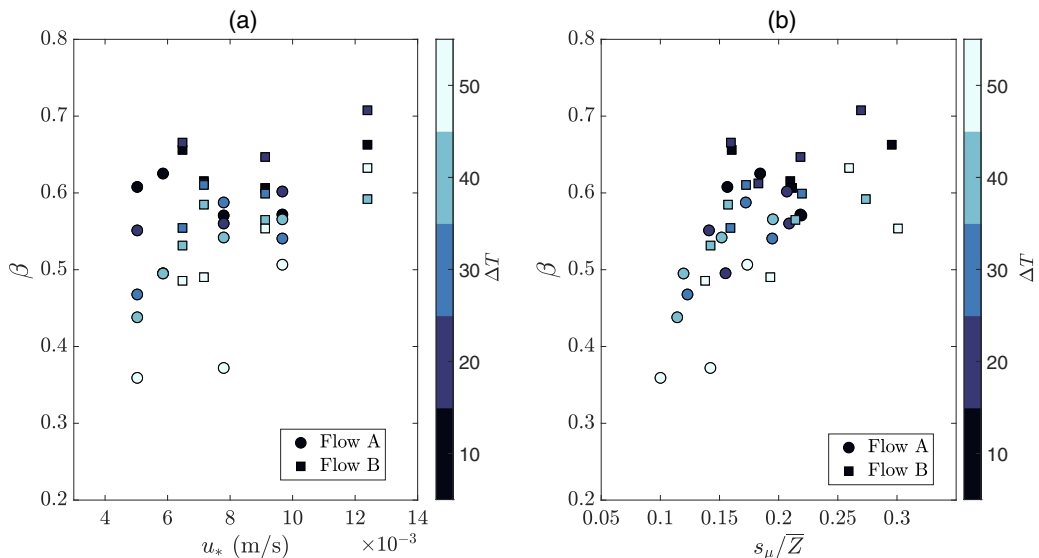


FIG. 13. (a) Entrainment coefficient, β versus the friction velocity, u_* . (b) Entrainment coefficient versus the variability, s_μ/\bar{Z} . Each marker color corresponds to different source plume temperature as found on the legend.

B, except to a small degree for the less turbulent cases ($X_p = 0.3$ and 0.6 m), no strong influence of the temperature differential can be observed.

The behavior observed for Flow A suggests that there are competing effects in play. The plume buoyancy seems to suppress or counteract the influence of canopy turbulence on plume variability. This effect may be due to two possible processes. First, because the stronger ΔT cases produce stronger local stratification, the plume may be able to resist the vertical movement and turbulent motions. In contrast, the case of $\Delta T = 10^\circ\text{C}$ is almost close to a scalar plume source, allowing unhindered influence of the canopy turbulence. Second, because the more heated plumes experience higher buoyancy, the plume may more preferentially/easily restore to a higher/natural plume rise height. This bias can limit the full range of variability. This trend is not observable for Flow B (faster, more turbulent) cases, suggesting that the turbulence is too strong and overcomes the suppression effect of the temperature differential. (The interaction of stratification with canopy turbulence is explored further in Sec. IV.)

3. Mixing and entrainment

Another important characteristic of plumes is mixing and entrainment, or in our case, the entrainment of momentum and ambient cooler fluid into the buoyant jet. Entrainment rates can control the plume's cooling/mixing and growth rates and therefore have strong implications for wildfire plume behavior and the fate/transport of embers. Substantial literature has shown that a plume under crosswind (bent-over) has a much higher entrainment rate than in quiescent conditions [17,18,26,28,29,31,35,56]. Because most systems with cross-flow or unstable atmospheric conditions experience significant turbulence, some work also looks at the influence of ambient turbulence on plume entrainment [20,21,31]. For our system, we aim to understand how the plume's oscillatory behavior under CSD turbulence impacts its rate of entrainment.

We extract the entrainment coefficient, β , from our data set as the rate at which the radius of the plume grows with height. A description of this method and estimates of β are discussed in Appendix A. Figures 13(a) and 13(b) plot the extracted entrainment coefficients for all the experimental cases against u_* and s_μ . In the former, we seek to find a relationship between the

turbulent state (u_*) and entrainment (β). We find that most of our β values range between 0.45 and 0.7. For comparison, previous studies of entrainment in buoyant plumes under cross-flow found values of β to be 0.45 in a hot water plume study [28], 0.4–0.5 in a numerical study [29], 0.55 for flames under wind [35], 0.57 [27], among others. While most of our β values fall within the typical range, the more turbulent and less buoyant cases experience higher entrainment rates.

As found previously, temperature (buoyancy) effects have a strong competing effect with turbulence on the plume’s oscillatory behavior. Therefore, the $\Delta T = 10^\circ\text{C}$ case essentially allows for isolation of the impact of turbulence only. The plot (black data points) shows that with limited buoyancy, the entrainment rate increases monotonically with increasing u_* . This shows that the CSD-induced oscillatory motion enhances mixing. For the other cases however, we are unable to find any clear trends. However, treating all the experimental cases together as a whole, we can see that there is a weak relationship between the entrainment rate and u_* . This may be because the oscillatory behavior that largely contributes to the mixing is dependent on the combined effect of the turbulence (u_*) and its suppression (ΔT).

To observe the influence of ΔT alone on the entrainment rate, we can look at β for the lowest u_* case for each Flow A (circles, at $u_* = 0.005$ m/s) and Flow B (squares, at $u_* = 0.0065$ m/s). In general, the lower ΔT data points (dark purple and black) populate the regions of higher beta, while that of higher ΔT (white and light blue) populate regions of lower β . In both flow cases we see that the entrainment increases with ΔT . This shows that with stronger temperature differentials (in absence of strong turbulence), mixing can be suppressed.

In Fig. 13(b), we plot β against s_μ/\bar{Z} (variability) to get a better sense of how β varies with the combined effects of source turbulence and temperature. s_μ/\bar{Z} in this plot is measured at $x_{dp} = 32.4$ cm. Similar trends are observed elsewhere along x_{dp} . We find that entrainment increases with increasing variability, close to linearly. However, more data points are needed at higher s_μ to confirm this apparent trend.

The findings from all three aspects of the plume characteristics (impacted by CSD) highlight how important the source conditions (both background CSD turbulence and temperature ΔT) are for the plume characteristics. Even though the plume mixes quite rapidly with the ambient and loses its initial heat, the source ΔT sets the characteristics of the whole plume. This matches past literature that found that behavior of forced plumes (heated jets) is strongly controlled and influenced by the source buoyancy and momentum fluxes [21–23,57]. Such manifestation of the source conditions can potentially alter conditions to be favorable or suppressive for wildfire spread.

IV. DISCUSSION

The plume source conditions have a large impact on the plume fate, behavior, and trajectory: specifically, we have found that the canopy turbulence at X_p in combination with plume source conditions determine the plume variability s_μ and entrainment rate β . Furthermore, the plume’s variability and oscillatory behavior is caused in a large part by the organized nature and coherent structures associated with the CSD, as seen in its properties. Because these characteristics can have potentially strong effects on wildfire spread and ember transport, it is important to understand under what conditions the plumes exhibit enhanced CSD effects.

A. Nondimensional power scaling for plume variability

As introduced in Sec. I, wildfire plumes can be characterized by nondimensional numbers such as N_c or Fr_c , which compare the power of the fire (plume/buoyancy) with the power of the wind [14,15,35,49]. Because these nondimensional parameters are transformed forms of water plume scaling to fit fire parameters, we use classic plume formulations for our study, expressed by Eq. (1). In our case, the Byram’s criterion would be $N_c = 2B_R/U_\infty^3$, in which B_R is the buoyancy flux. The buoyancy flux is given by $B_R = g\Delta\rho q/\rho_a$, in which we calculate ρ , and $\Delta\rho$ based on the plume source and ambient temperature. All the temperature and velocity scales are based on source

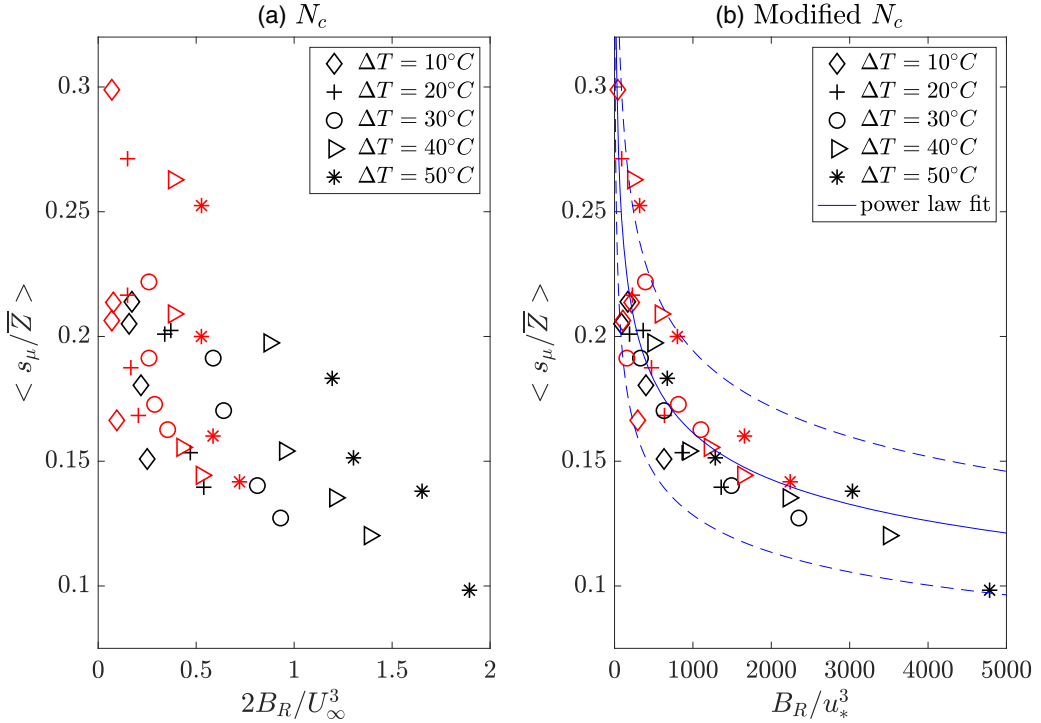


FIG. 14. (a) Plot of s_μ/\bar{Z} averaged over $z_{dp} = 32$ to 36 cm against nondimensional quantity $N_c = 2B_R/(U_\infty^3)$. Black and red symbols correspond to Flow A and B. Each symbol shape correspond to different source temperature, as on legend. (b) Same plot repeated for the altered power comparison, B_R/u_*^3 . The blue line provides a power-law fit of $s_\mu/\bar{Z} = a * (B_R/u_*^3)^b$ for which $a = 0.55$ and $b = -0.22$. The fit gives an R^2 value of 0.75 . The dotted lines are for a values within 95% confidence interval.

conditions. This includes the free-stream velocity, U_∞ , for which we use the velocity measured right above the source at X_p . We use this formulation of N_c in Fig. 14(a), in which we plot N_c against a measure of the plume variability, s_μ . N_c is shown on the x axis with increasing values indicating an increasing influence of buoyancy. Our experimental cases range from 0.07 to 2 : Those with $N_c < 1$ are regarded in the wildfire literature as “wind driven” and those with $N_c > 1$ are regarded as buoyancy dominated. This range of values of N_c covers more wind-driven cases by design. This is because higher wind velocities are required to observe the formation of CSD structures and turbulence.

Because these parameters (N_c) have more typically been used in the past for predicting the rate of spread of wildfires, it is not surprising that no strong trends with N_c are evident here when focusing on plume variability. That said, there is a very general trend that the variability increases with higher windspeed, which is because higher turbulence is experienced at higher velocities. However, because our cross-flow does not change within each set of A and B conditions, the velocities (U_∞) change minimally despite the turbulent Reynolds stresses varying greatly with changing X_p . Therefore, the current characterization of wildfire plumes based on N_c is inadequate for predicting s_μ and β , which both can have strong implications for wildfire spread.

We have found previously that s_μ (and/or β) is dependent on the competing effects of buoyancy (ΔT) and canopy turbulence (u_*). Therefore, we suggest a new scaling similar to N_c that compares the buoyancy to friction velocity instead of the free-stream velocity. We replace U_∞ with u_* and plot against s_μ in Fig. 14(b). The black data points are for Flow A while the red points are for Flow B. Increasing B_R/u_*^3 signifies the increasing effect of buoyancy or decreasing turbulence.

The new scaling collapses the different experimental cases, including both flow cases, quite well. We find that with increasing B_R/u_*^3 , s_μ decreases at a decreasing rate. Figure 14(b) provides a best power-law fit in blue, although more data points are necessary to improve this fit. The power law follows an exponent value of -0.2 . This is because near B_R/u_*^3 of zero, there is little influence of buoyancy, and the plume variability is set by the turbulence and the canopy roller dynamics near the source. Although we do not have a data point to corroborate this, an upper limit that creates fluctuations of amplitude equivalent to the maximum plume height ($s_\mu/\bar{Z} = 1$) may be possible with a much bigger/intense canopy roller. At the opposite limit, we find that with little ambient turbulence and the restrictions on vertical fluctuations imposed by the buoyancy, the variability will be limited to the base level of variability found in plumes under cross-flow with no CSD. In this case the turbulence contributing to u_* will instead be due to the shear between the plume/jet and ambient rather than the canopy shear dynamics. Because the jet is also turbulent, the decay will not be to zero, but in our case to a s_μ/\bar{Z} of 0.1 to 0.12.

While this scaling does better predict the oscillatory behavior of the plume, it is important to note that u_* is a combined effect of the canopy drag and ambient crosswind. In other words, because a faster flow through a sufficiently dense canopy will create stronger turbulence (u_*), there may be some cases in which the U_∞ based scaling will correlate well with estimates of plume variability. However, in our experimental cases, because the cross-flow velocity remains mostly the same while the canopy length contribute to the level of turbulence, the u_* scaling is more appropriate.

B. Richardson scaling

We have shown scaling comparisons based on power, length, and velocity. In an earlier section, as portrayed in Fig. 13, we found that there is a strong dependency of observed variability on ΔT for fixed X_p . Because of possible stabilizing effects on the variability of the plume by buoyancy, a Richardson number scaling may be relevant here. We define a bulk Richardson number by

$$\text{Ri}_b = g\beta_T \frac{\Delta T}{L_{\text{pl}}} \tau^2. \quad (3)$$

The term $g\beta_T(\frac{\Delta T}{L_{\text{pl}}})$ is equivalent to the Brunt Väisälä frequency, N^2 , where g is the gravitational constant, β_T is the thermal expansion coefficient for water, ΔT is the source temperature difference, and L_{pl} is the plume length scale. The plume length scale, defined as the vertical length traveled by the plume over one KH-roller cycle is dependent on the average plume rise velocity, w_{eff} (described in Appendix B). τ is the time scaling for the canopy induced turbulence given by $\tau = L_{\text{RS}}/u_*$. L_{RS} is the length scale related to the RS profiles on Fig. 4. It is defined as starting at the height of maximum Reynolds stress (usually at the velocity inflection point), and ending at the height at which the Reynolds stress decays to 10% of the maximum RS.

Figure 15 plots both plume height variability and entrainment against the bulk Richardson number. These plots show how variability and mixing change with stratification and the ambient turbulence. However, we emphasize that the stratification referred to in this section and parameterized by the Ri_b is not associated with ambient atmosphere stratification as in many wildfire or plume literature. Instead, it refers to the observable buoyancy effects at the interface between the heated plume and the ambient fluid, or the resistance of the buoyant plume to turbulent perturbations. The trends that we observe with Ri_b is similar to that found for the power scaling (N_c). As the stratification effects become stronger (Ri_b increases), the variability decreases to a plateau [Fig. 15(a)]. Overall, the observed variability decreases at a decreasing rate with increasing Ri_b . The entrainment, β , also decreases with increasing Ri_b . Both relationships highlight that increasing effects of stratification are capable of suppressing the plume response to canopy turbulence.

C. Implications for spotfire initiation

Spotfire spread refers to the lofting and transport of burning firebrands by plumes under crosswinds. These firebrands are capable of starting new fires far downwind of the main fire. Spotfires

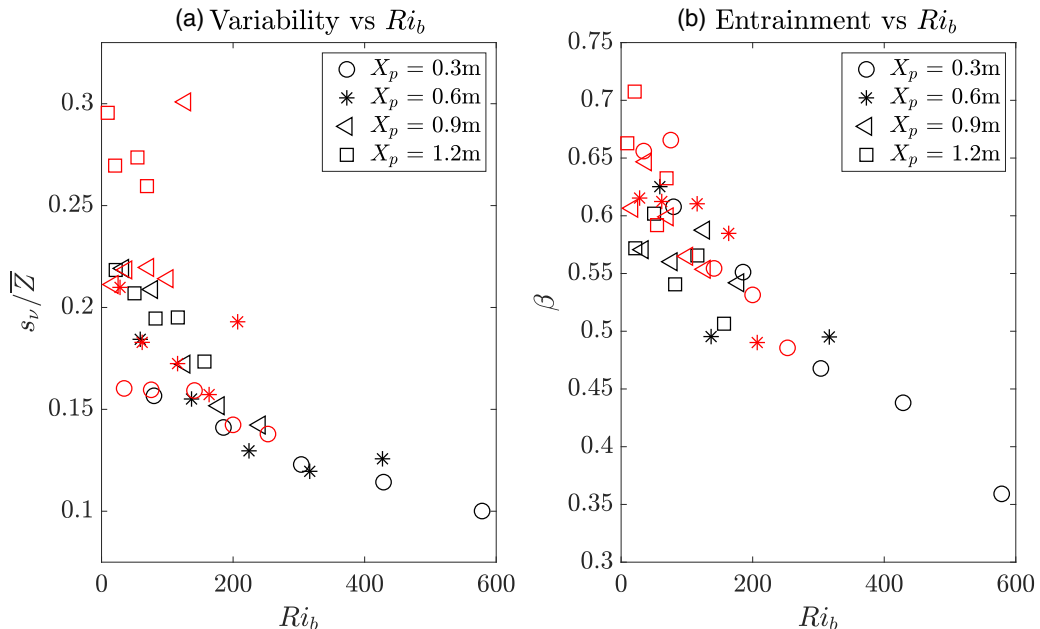


FIG. 15. Bulk Richardson scaling against s_μ and β . The black markers correspond to Flow A while the red markers correspond to Flow B. Each marker symbol corresponds to different X_p , as in the legend. We have omitted outlier data points from cases A06dT30, A06dT50, A09dT50, and B12dT30.

are already very hard to contain because of the large variability in how they spread. Because buoyant plumes are responsible for spotfires, any variability in their trajectory can exacerbate the predictability of their spread. Therefore, by oscillating the path of the plume over a larger vertical range, the CSD is essentially making the trajectories of the firebrands more extreme and dispersed. For example, we have observed that instantaneous plume paths are both far higher and far lower than the mean path under no strong ambient turbulence. As a result, a fraction of the embers can be intermittently lofted higher to sample higher windspeeds that carry them much further downwind. Similarly, some of the embers will be lofted to lower heights and will not travel as far thus increasing the variability in ember travel distance. This prompts the need to better understand the role of CSD in wildfire dynamics to inform wildfire management decisions.

V. CONCLUSIONS

We have presented results from an experimental study that clearly illustrates the importance of CSD on buoyant plume behavior. We have confirmed that CSD can have a strong impact on plume behavior, which manifests itself as strong oscillatory behavior at the frequency of the canopy K-H instability. This response is specific to CSD and associated large-scale coherent structures, and not like other sources of ambient turbulence. Furthermore, we have found that while source turbulence and buoyancy conditions set the frequency and intensity of these oscillations, the flow perturbations propagate through the plume at the free-stream velocity. We have also found that this oscillatory behavior is a product of two competing behaviors: the CSD rollers that enhance it and the buoyancy (temperature differential) that suppresses it. This competing behavior can be parameterized by nondimensional numbers in the form of a modified Byram's criterion (N_c) that uses a turbulent velocity scaling (u_*) instead of the free-stream velocity. We found that for our experimental parameters, which fall in cross-flow dominated flow regimes, the plume variability

follows a decaying power-law relationship with increasing B_R/u_*^3 . Which means that with higher turbulence and weaker buoyancy, variability increases, and vice versa.

While none of these findings directly connect the influence of CSD to wildfire rate of spread and how it may be exacerbated/mediated, they do highlight how variable and unpredictable the plume behavior becomes in the presence of canopy rollers. This is important because from the perspective of wildfire management, unpredictability and uncertainty are major hurdles to containment. Our results show that with enhanced CSD, the plume heights/trajectories become more extreme, and thereby, can have a strong impact on spotfire spread.

Clearly, while our study has provided an important start to understanding this issue, more work needs to be done to better understand these dynamics. A wider range of experimental parameters, such as U_∞ , source dimensions, q , and ΔT can provide more data points for the different scaling relationships we have tested in the discussion section. Additionally, numerical studies can offer more accurate values of quantities such as β , temperature fields, or trajectories. Furthermore, we need to understand how these plumes under CSD interact with canopy gaps/edges. Because wildfire spread does occur across fuel breaks, gaps in the canopy, or from forest edges downstream, understanding the plume interaction with canopy edges is crucial to better understanding spotfire spread.

ACKNOWLEDGMENTS

This research project was made possible through funding from the Stanford CEE Leavell fellowship, Stanford Graduate Fellowship, the Stanford Woods Institute for the Environment, and the Stanford Bill Lane center for the American West.

APPENDIX A: ENTRAINMENT COEFFICIENT EXTRACTION

The entrainment coefficient, β , used in Sec. III C 3 can be estimated by approximating the rate at which the radius of the plume $R(x_{dp})$ grows with height $[\mu(x_{dp})]$ [28,29]. Previous studies find that a buoyant plume's radius increases linearly with vertical distance [22]. Therefore, an entrainment coefficient, β , can be calculated by the relation:

$$R(x) = R_0 + \beta * [\mu(x) - \mu_0], \quad (A1)$$

where $R(x)$ is the radius of the plume, R_0 is the initial plume radius, $\mu(x)$ is the elevation of the plume trajectory above the bed, and μ_0 is the height of plume release. We can fit a linear fit to a sample data set of $R(x)$ vs $\mu(x)$. The slope of the linear fit gives us an estimate of β for each experimental case. We define $R(x) = 2\sigma(x)$, which is calculated using moments of the dot-pattern vertical distribution as described in the methodology (Sec. II B). We plot $R(x)$ vs $\mu(x)$

TABLE II. Entrainment fit values. For each experimental case, we provide β , the slope of the linear fit to R vs μ , and its corresponding R^2 values. n/a are for bad fits that are omitted from the β data set.

Case	β	R^2	Case	β	R^2	Case	β	R^2	Case	β	R^2
A03dT10	0.61	0.93	A06dT10	0.63	0.87	B03dT10	0.66	0.94	B06dT10	0.62	0.95
A03dT20	0.55	0.93	A06dT20	0.50	0.81	B03dT20	0.67	0.91	B06dT20	0.61	0.92
A03dT30	0.47	0.92	A06dT30	n/a	n/a	B03dT30	0.55	0.84	B06dT30	0.61	0.80
A03dT40	0.44	0.94	A06dT40	0.49	0.90	B03dT40	0.53	0.82	B06dT40	0.58	0.76
A03dT50	0.36	0.95	A06dT50	n/a	n/a	B03dT50	0.48	0.82	B06dT50	0.49	0.80
A09dT10	0.57	0.95	A12dT10	0.57	0.93	B09dT10	0.61	0.93	B12dT10	0.66	0.95
A09dT20	0.56	0.94	A12dT20	0.60	0.93	B09dT20	0.65	0.90	B12dT20	0.71	0.95
A09dT30	0.59	0.90	A12dT30	0.54	0.93	B09dT30	0.60	0.83	B12dT30	n/a	n/a
A09dT40	0.54	0.94	A12dT40	0.57	0.95	B09dT40	0.56	0.80	B12dT40	0.59	0.87
A09dT50	0.37	0.96	A12dT50	0.51	0.95	B09dT50	0.55	0.79	B12dT50	0.63	0.86

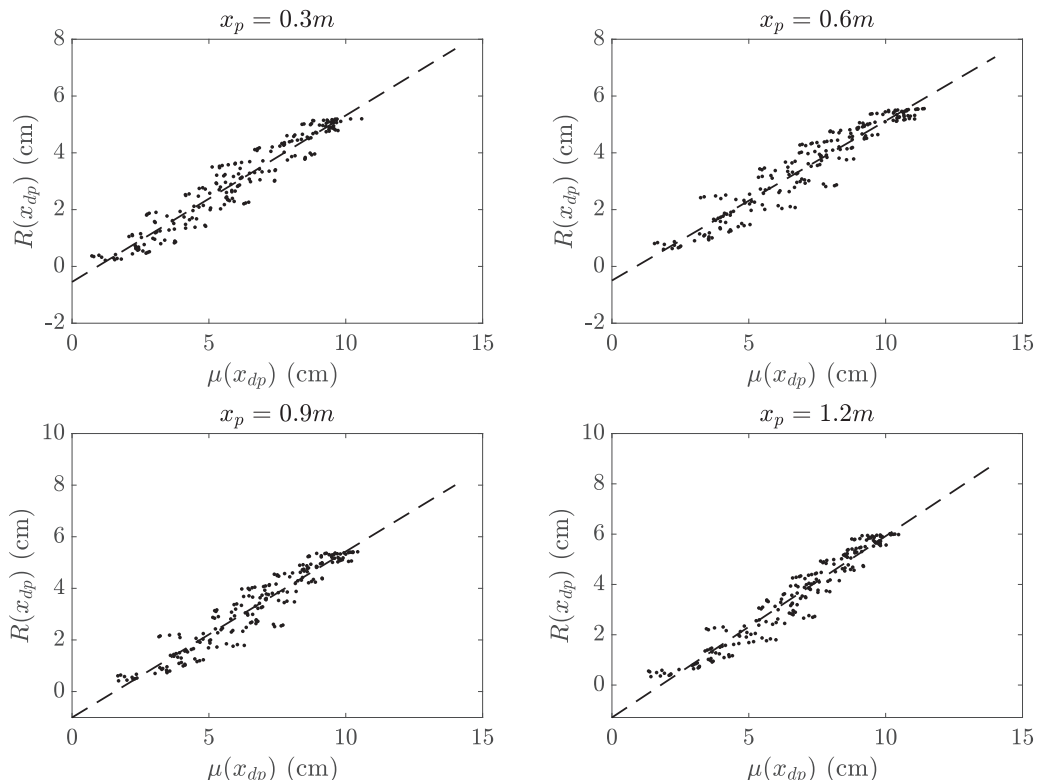


FIG. 16. Plots of plume radius, $R(x)$, vs the plume height given defined by the centerline, μ . All of the provided plots are for experimental cases with $\Delta T = 50^\circ\text{C}$ and cross-flow setting of Flow A. Each subplot corresponds to different X_p conditions as denoted in the title. The black dashed lines are linear fits to the data points.

with corresponding linear fits for Flow A and $\Delta T = 50^\circ\text{C}$ in Fig. 16. Each subplot corresponds to different sample X_p cases. Most of the linear fits give an estimate of β with an R^2 value of above 0.9 for Flow A and above 0.8 for Flow B. The values of β and corresponding R^2 values are given in Table II.

APPENDIX B: PLUME LENGTH SCALE

In order to calculate Ri_b in Sec. IV B, we needed a plume length scale. To estimate L_{pl} of the plume, we approximated the vertical length over which the plume travels within one canopy roller (KH cycle) period. For fully developed flow, f_{KH} is 0.14 s^{-1} and 0.18 s^{-1} for Flows A and B, respectively. To approximate the vertical distance the plume travels within this time, we use a mean vertical velocity in which fluid is transported through the plume. We call this speed w_{eff} , or effective vertical velocity to calculate:

$$L_{\text{pl}} = w_{\text{eff}} * (1/f_{\text{KH}}). \quad (\text{B1})$$

We use w_{eff} instead of the source velocity, because while the source velocity sets the characteristics of the plume, there is considerable entrainment of ambient fluid initially which needs to be accounted for in an effective vertical velocity. To derive this effective velocity, we can utilize a kinematic relationship for plume rise [26,29,31] that provides a vertical plume velocity that is

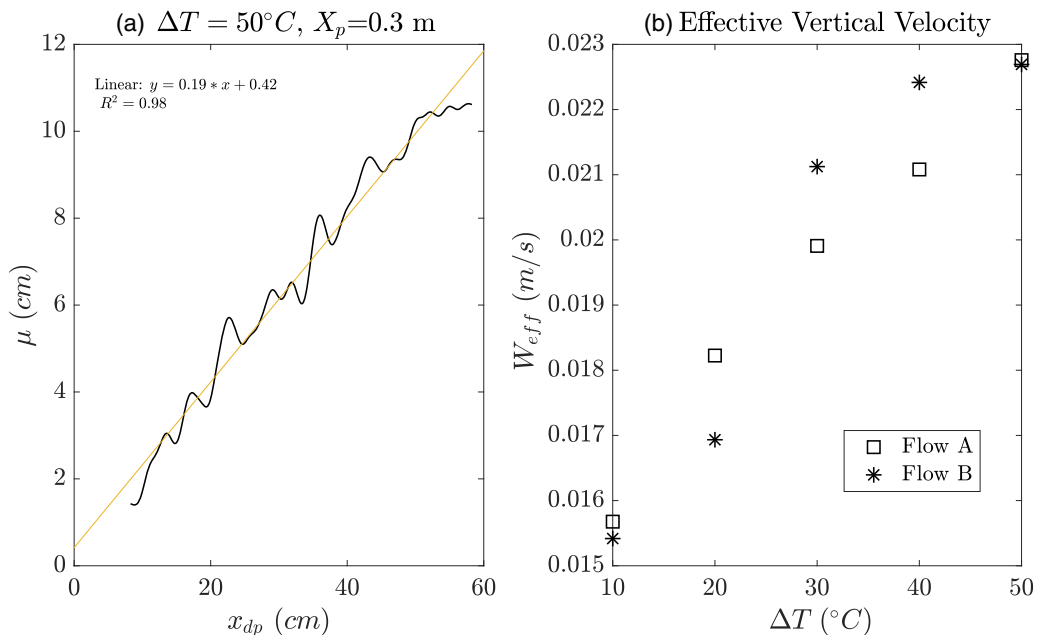


FIG. 17. (a) Example of w_{eff} extraction. A linear fit is provided in red, to the time mean trajectory, $\mu(x_{dp})$, for the A03dT50 case. (b) The extracted w_{eff} plotted for both Flow A and B (as on legend) across different ΔT . The values for extracted for experimental cases of $X_p = 0.3\text{ m}$. Other X_p have similar effective velocities because mean trajectory are similar as shown on Fig. 5.

averaged across the plume:

$$\frac{d\bar{Z}}{dx} = w_{\text{eff}}/U. \quad (\text{B2})$$

U in the expression above is the background cross flow velocity, and Z is the height of the plume at some distance downstream x_{dp} . The slope, $\frac{d\bar{Z}}{dx}$, can be found by fitting a linear curve to the mean centerline trajectory of a plume (μ vs x_{dp}). An example of this can be seen in Fig. 17(a). For the cross-flow velocity U , we can use U_∞ . This slope then can be used to extract w_{eff} . We extract w_{eff} for all $X_p = 0.3\text{ m}$ (limited turbulence cases), as plotted in Fig. 17(b). We see that for both Flow A and B, the w_{eff} increases with increasing source buoyancy, as expected. We also find a good agreement in values of w_{eff} for Flow A and B. This is a good measure to show that our inlet momentum condition (through the constant flow rate) is consistent across experimental cases.

APPENDIX C: PLUME CENTERLINE ERROR

As mentioned with the mean trajectories, estimates of the plume centerline (μ) is somewhat biased for some of the experimental cases. This is because in the more turbulent Flow B cases, as the plume is swept up and down, there are instances when the lower part of the plume is pushed downward into the canopy. Specifically, with the shorter distance between the plume bottom and canopy top (for Flow B), the fluctuations and vertical movements of the plume periodically force the plume downward into the canopy array. Because we are unable to track the plume through the solid canopy elements, this results in a bias in our estimates of μ (overapproximation) and R (underapproximation). However, this does not alter the finding that the plume moves with increasing variability in the presence of canopy-induced turbulence. Furthermore, we confirmed that the bias is not significant enough to influence other quantities observed for this study.

To confirm that the error is not significant (in Flow B cases), we estimated the fraction of the experiment duration (7 min) that the plume may fall below the canopy height. The upper edge of the canopy, $z_{pt}(x_{dp})$, can be determined accurately because it does not fall below the canopy height at any instant in all of the experimental cases. Furthermore, the thickness of the plume [$R(x_{dp})$] does not vary by more than ± 1 cm over the time record. Therefore, we can subtract the mean thickness of the plume, $\overline{R(x_{dp})}$ from each instance of the plume upper edge, $z_{pt}(x_{dp})$, to get a rough estimate of the bottom edge of the plume at any given time. Given that $R = 2\sigma$ and the total vertical length would be 4σ , we calculated the percentage of the time that $z_{pt} - 4\sigma < 0$ and $z_{pt} - 2\sigma < 0$. The former estimates the amount of time that the plume bottom just touches the top of the canopy, while the latter estimates the amount of the time when over half of the plume falls below the canopy height. We find that the plume just touches the canopy top roughly 36% and 47% for $X_p = 0.3$ m and $X_p = 1.2$ m, respectively, while the plume is pushed over halfway into the canopy roughly 1% and 4.5% of the time for the same cases. This suggests that our estimates for the location of the centerline of the plume is somewhat inaccurate for only roughly 4.5% of the frames under strong turbulence. Furthermore, the fact that plumes just touch the canopy top, or slightly enters the canopy should not affect our estimate of μ or R a great deal.

-
- [1] K. Collins, O. F. Price, and T. D. Penman, Spatial patterns of wildfire ignitions in south-eastern Australia, *Int. J. Wildl. Fire* **24**, 1098 (2015).
- [2] S. Marques, J. G. Borges, J. Garcia-Gonzalo, F. Moreira, J. M. B. Carreiras, M. M. Oliveira, A. Cantarina, B. Botequim, and J. M. C. Pereira, Characterization of wildfires in Portugal, *Eur. J. Forest Res.* **130**, 775 (2011).
- [3] X. Úbeda and P. Sarricolea, Wildfires in Chile: A review, *Glob. Planet. Change* **146**, 152 (2016).
- [4] J. Miller, H. Safford, M. Crimmins, and A. E. Thode, Quantitative evidence for increasing forest fire severity in the Sierra Nevada and Southern Cascade Mountains, *Ecosystems* **12**, 16 (2009).
- [5] A. Westerling, H. Hidalgo, D. R. Cayan, and T. W. Swetnam, Warming and earlier spring increase western US forest wildfire activity, *Science* **313**, 940 (2006).
- [6] D. E. Calkin, M. P. Thompson, and M. A. Finney, Negative consequences of positive feedbacks in US wildfire management, *For. Ecosyst.* **2**, 9 (2015).
- [7] B. E. Potter, Atmospheric interactions with wildland fire behaviour - II. Plume and vortex dynamics, *Int. J. Wildl. Fire* **21**, 802 (2012).
- [8] R. N. Meroney, Fires in porous media: natural and urban canopies, in *Flow and Transport Processes with Complex Obstructions*, NATO Science Series, Vol. 236, edited by Y. A. Gayev and J. C. Hunt (Springer, Dordrecht, 2007), pp. 271–310.
- [9] M. T. Kiefer, Y.-L. Lin, and J. J. Charney, A study of two-dimensional dry convective plume modes with variable critical level height, *J. Atmos. Sci.* **65**, 448 (2008).
- [10] F. A. Albini, Spot fire distance from burning trees: a predictive model, Intermountain Forest and Range Experiment Station, Forest Service, US Department of Agriculture, General Technical Report INT-GTR-56 (1979).
- [11] C. Tarifa, P. Notario, F. Moreno, and A. Villa, Transport and combustion of firebrands, Final Report of Grants FG-SP-114 and FG-SP-146 (Vol. II) (1967).
- [12] H. B. Clements, *Lift-off of Forest Firebrands* (USDA Forest Service Southeastern Forest Experiment Station, Asheville, NC, 1977), Vol. SE-159
- [13] M. A. Storey, O. F. Price, M. Almeida, C. Ribeiro, R. A. Bradstock, and J. J. Sharples, Experiments on the influence of spot fire and topography interaction on fire rate of spread, *PLoS One* **16**, e0245132 (2021).
- [14] G. Byram, Combustion of forest fuels, in *Forest Fire: Control and Use*, edited by K. Davis (McGraw-Hill, New York, 1959).

- [15] R. M. Nelson, Byram derivation of the energy criterion for forest and wildland fires, *Int. J. Wildl. Fire* **3**, 131 (1993).
- [16] R. M. Nelson, Power of the fire—A thermodynamic analysis, *Int. J. Wildl. Fire* **12**, 51 (2003).
- [17] D. P. Hault, J. A. Fay, and L. J. Forney, A theory of plume rise compared with field observations, *J. Air Pollut. Contr. Assoc.* **19**, 585 (1969).
- [18] A. Tohidi and N. B. Kaye, Highly buoyant bent-over plumes in a boundary layer, *Atmos. Environ.* **131**, 97 (2016).
- [19] P. R. Slawson and G. T. Csanady, The effect of atmospheric conditions on plume rise, *J. Fluid Mech.* **47**, 33 (1971).
- [20] S. J. Wright, The effect of ambient turbulence on jet mixing, in *Recent Research Advances in the Fluid Mechanics of Turbulent Jets and Plumes*, edited by P. A. Davies and M. J. Valente Neves (Kluwer Academic Publishers, Dordrecht, 1994), pp. 13–27.
- [21] A. Matulka, P. López, J. M. Redondo, and A. Tarquis, On the entrainment coefficient in a forced plume: Quantitative effects of source parameter, *Nonlin. Process. Geophys.* **21**, 269 (2014).
- [22] B. R. Morton, Forced plumes, *J. Fluid Mech.* **5**, 151 (1958).
- [23] B. R. Morton, G. I. Taylor, and J. S. Turner, Turbulent gravitational convection from maintained and instantaneous sources, *Proc. R. Soc. A* **234**, 1 (1956).
- [24] P. R. Slawson and G. T. Csanady, On the mean path of buoyant, bent-over chimney plumes, *J. Fluid Mech.* **28**, 311 (1967).
- [25] L.-N. Fan, Turbulent buoyant jets into stratified or flowing ambient fluids, *Clin-Alert* **5**, 45 (1967).
- [26] D. P. Hault and J. C. Weil, Turbulent plume in a laminar cross flow, *Atmos. Environ.* **6**, 513 (1972).
- [27] E. J. List, Turbulent jets and plumes., *Annu. Rev. Fluid Mech.* **14**, 189 (1982).
- [28] B. W. Alton, G. A. Davidson, and P. R. Slawson, Comparison of measurements and integral model predictions of hot water plume behaviour in a crossflow, *Atmos. Environ. Part A Gen. Top.* **27**, 589 (1993).
- [29] B. J. Devenish, G. G. Rooney, H. N. Webster, and D. J. Thomson, The entrainment rate for buoyant plumes in a crossflow, *Bound.-Layer Meteorol.* **134**, 411 (2010).
- [30] P. J. Roberts, Line plume and ocean outfall dispersion, *ASCE J. Hydraul. Div.* **105**, 313 (1979).
- [31] G. Briggs, Plume Rise, AEC Critical Review Series, TID-25075 (1969), <https://www.osti.gov/servlets/purl/47431>.
- [32] M. T. Kiefer, M. D. Parker, and J. J. Charney, Regimes of dry convection above wildfires: Idealized numerical simulations and dimensional analysis, *J. Atmos. Sci.* **66**, 806 (2008).
- [33] A. L. Sullivan, Convective froude number and byram's energy criterion of Australian experimental grassland fires, *Proc. Combust. Inst.* **31**, 2557 (2007).
- [34] G. N. Mercer and R. O. Weber, Plumes above line fires in a cross-wind, *Int. J. Wildl. Fire* **4**, 201 (1994).
- [35] R. M. Nelson, B. W. Butler, and D. R. Weise, Entrainment regimes and flame characteristics of wildland fires, *Int. J. Wildl. Fire* **21**, 127 (2012).
- [36] P. Werth, B. Potter, and C. Clements, Synthesis of knowledge of extreme fire behavior: Volume I for fire managers, Gen. Tech. Rep. PNW-GTR- 854. Portland, OR: US Department of Agriculture, Forest Service, Pacific Northwest Research Station, 144 p (2011).
- [37] J. Finnigan, Turbulence in plant canopies, *Annu. Rev. Fluid Mech.* **32**, 519 (2000).
- [38] M. R. Raupach, J. J. Finnigan, and Y. Brunet, Coherent eddies and turbulence in vegetation canopies: The mixing-layer analogy, in *Boundary-Layer Meteorology 25th Anniversary Volume, 1970–1995*, edited by J. R. Garratt and P. A. Taylor (Springer, Dordrecht, 1996), pp. 351–382.
- [39] M. R. Raupach and A. S. Thom, Turbulence in and above plant canopies, *Annu. Rev. Fluid Mech.* **13**, 97 (2003).
- [40] M. Ghisalberti and H. M. Nepf, The limited growth of vegetated shear layers, *Water Resour. Res.* **40**, W07502 (2004).
- [41] M. Ghisalberti and H. Nepf, Mass transport in vegetated shear flows, *Environ. Fluid Mech.* **5**, 527 (2005).
- [42] H. Nepf and M. Ghisalberti, Flow and transport in channels with submerged vegetation, *Acta Geophys.* **56**, 753 (2008).

- [43] M. T. Kiefer, W. E. Heilman, S. Zhong, J. J. Charney, and X. Bian, A study of the influence of forest gaps on fire-atmosphere interactions, *Atmos. Chem. Phys.* **16**, 8499 (2016).
- [44] M. T. Kiefer, S. Zhong, W. E. Heilman, J. J. Charney, and X. Bian, A numerical study of atmospheric perturbations induced by heat from a wildland fire: Sensitivity to vertical canopy structure and heat source strength, *J. Geophys. Res.: Atmos.* **123**, 2555 (2018).
- [45] D. Morvan, Physical phenomena and length scales governing the behaviour of wildfires: A case for physical modelling, *Fire Technol.* **47**, 437 (2011).
- [46] D. Morvan, G. Accary, S. Meradji, N. Frangieh, and O. Bessonov, A 3D physical model to study the behavior of vegetation fires at laboratory scale, *Fire Saf. J.* **101**, 39 (2018).
- [47] M. El Houssami, A. Lamorlette, D. Morvan, R. M. Hadden, and A. Simeoni, Framework for submodel improvement in wildfire modeling, *Combust. Flame* **190**, 12 (2018).
- [48] F. Pimont, J. L. Dupuy, R. R. Linn, and S. Dupont, Impacts of tree canopy structure on wind flows and fire propagation simulated with FIRETEC, *Ann. For. Sci.* **68**, 523 (2011).
- [49] R. C. Rothermel, Predicting behavior and size of crown fires in the Northern Rocky Mountains, US Department of Agriculture, Forest Service, Intermountain Forest and Range Experiment Station, **43** (1991), <https://doi.org/10.2737/INT-RP-438>.
- [50] F. Morandini, X. Silvani, F. Morandini, and X. Silvani, Experimental investigation of the physical mechanisms governing the spread of wildfires, *Int. J. Wildl. Fire* **19**, 570 (2010).
- [51] M. Ghisalberti and H. Nepf, The structure of the shear layer in flows over rigid and flexible canopies, *Environ. Fluid Mech.* **6**, 277 (2006).
- [52] Z. Chen, C. Jiang, and H. Nepf, Flow adjustment at the leading edge of a submerged aquatic canopy, *Water Resour. Res.* **49**, 5537 (2013).
- [53] H. Chung, T. Mandel, F. Zarama, and J. R. Koseff, Local and nonlocal impacts of gaps on submerged canopy flow, *Water Resour. Res.* **57**, e2019WR026915 (2021).
- [54] G. S. Settles and M. J. Hargather, A review of recent developments in schlieren and shadowgraph techniques, *Meas. Sci. Technol.* **28**, 042001 (2017).
- [55] R. H. Shaw, J. Tavangar, and D. P. Ward, Structure of the Reynolds stress in a canopy layer, *J. Appl. Meteorol. Climatol.* **22**, 1922 (1983).
- [56] F. A. Albini, A model for the wind-blown flame from a line fire, *Combust. Flame* **43**, 155 (1981).
- [57] J. Turner, Buoyant plumes and thermals, *Annu. Rev. Fluid Mech.* **1**, 29 (1969).